



**MITIGATING THE MULTIPATH EFFECTS  
ON RADIO TOMOGRAPHIC IMAGING**

THESIS

Destinee N. Battle, 1<sup>st</sup> Lt, USAF

AFIT-ENG-MS-21-M-012

**DEPARTMENT OF THE AIR FORCE  
AIR UNIVERSITY**

***AIR FORCE INSTITUTE OF TECHNOLOGY***

**Wright-Patterson Air Force Base, Ohio**

DISTRIBUTION STATEMENT A  
APPROVED FOR PUBLIC RELEASE; DISTRIBUTION UNLIMITED.

The views expressed in this document are those of the author and do not reflect the official policy or position of the United States Air Force, the United States Department of Defense or the United States Government. This material is declared a work of the U.S. Government and is not subject to copyright protection in the United States.

AFIT-ENG-MS-21-M-012

MITIGATING THE MULTIPATH EFFECTS ON RADIO TOMOGRAPHIC  
IMAGING

THESIS

Presented to the Faculty  
Department of Electrical and Computer Engineering  
Graduate School of Engineering and Management  
Air Force Institute of Technology  
Air University  
Air Education and Training Command  
in Partial Fulfillment of the Requirements for the  
Degree of Master of Science in Electrical Engineering

Destinee N. Battle, B.S.E.E.

1<sup>st</sup> Lt, USAF

March 25, 2021

DISTRIBUTION STATEMENT A  
APPROVED FOR PUBLIC RELEASE; DISTRIBUTION UNLIMITED.

AFIT-ENG-MS-21-M-012

MITIGATING THE MULTIPATH EFFECTS ON RADIO TOMOGRAPHIC  
IMAGING  
THESIS

Destinee N. Battle, B.S.E.E.  
1<sup>st</sup> Lt, USAF

Committee Membership:

Richard K. Martin, Ph.D  
Chair

Robert F. Mills, Ph.D  
Member

Michael A. Temple, Ph.D  
Member

## Abstract

Radio tomographic imaging (RTI) is a device-free localization (DFL) technology that utilizes a wireless sensor network (WSN) to create images based on attenuation caused by targets obstructing WSN signal propagation. The sensors use radio waves to transmit and receive signals and the RTI system collects the received signal strength (RSS) measurements to use for attenuation image generation. The radio waves allow the RTI system to detect targets through dense mediums such as smoke and walls. Although radio frequency (RF) signal transmission has benefits, it also introduces the issue of multipath propagation or interference. One main detriment of multipath interference is that it presents imaging artifacts in the attenuation images. These artifacts can lead to degraded image and target localization accuracy.

Various RTI models and reconstruction methods are equipped with capabilities to mitigate the effects of multipath interference. This thesis combined the network shadowing (NeSh) and weighting-g models in conjunction with Tikhonov regularization and low-rank and sparse decomposition (LRSD). MATLAB was used to implement the four combinations for six experimental data sets and produce attenuation images. The attenuation images were analyzed qualitatively and quantitatively to accomplish the goal of determining which combination performed best at locating human targets.

After analyzing the results, it was determined that no single combination outperformed the others for at least three out of the five quantitative metrics. Therefore, a rating technique was used instead to normalize the average results of each metric and find the mean across each combination's newly normalized average results. In accordance with the normalization scale, the lowest and best rating revealed the optimum combination was the weighting-g model implemented in conjunction with LRSD.

## Acknowledgements

I would like to thank my advisor, Dr. Richard Martin, for all of his helpful guidance and feedback throughout this process. I would like to thank the members of my committee for offering their time. I would also like to thank my loving boyfriend and family for all of their unending support!

Destinee N. Battle

# Table of Contents

	Page
Abstract .....	iv
Acknowledgements .....	v
List of Figures .....	viii
List of Tables .....	x
I. Introduction .....	1
1.1 Problem Background .....	1
1.1.1 Multipath Interference .....	1
1.1.2 RTI Models and Reconstruction Methods .....	2
1.2 Research Objectives .....	2
1.3 Document Overview .....	3
II. Background and Literature Review .....	4
2.1 Radio Tomographic Imaging .....	4
2.1.1 Wireless Sensor Network .....	5
2.1.2 Linear Formulation .....	7
2.1.3 Noise .....	9
2.2 RTI Models .....	10
2.2.1 Network Shadowing Model .....	10
2.2.2 Inverse Area Elliptical Model .....	12
2.2.3 Exponential-Rayleigh Model .....	14
2.2.4 Weighting-g Model .....	16
2.3 RTI Reconstruction Methods .....	17
2.3.1 Tikhonov Regularization .....	18
2.3.2 Heterogeneous Bayesian Compressive Sensing .....	19
2.3.3 Feedback-Based Sparse Bayesian Learning .....	21
2.3.4 Low-Rank and Sparse Decomposition .....	23
2.4 Target Localization .....	25
2.4.1 Single Target Localization .....	25
2.4.2 Multi-Target Localization .....	26
III. Methodology .....	29
3.1 RTI Models Chosen .....	29
3.2 RTI Reconstruction Methods Chosen .....	30
3.3 Performance Metrics .....	30
3.3.1 Image Mean-Squared Error .....	31
3.3.2 Dispersion .....	31

	Page
3.3.3 Target Location Root-Mean-Squared Error .....	32
3.3.4 Execution Time .....	33
3.4 RTI Parameters Chosen .....	33
3.4.1 Regularization Parameter .....	34
3.4.2 Width of the Ellipse .....	34
3.5 Cylindrical Human Model .....	40
3.6 RTI Data Collection .....	41
3.7 K-Means++ .....	42
IV. Results and Analysis .....	44
4.1 Attenuation Image Results .....	44
4.1.1 Target Location (9,14) .....	44
4.1.2 Target Location (5,5) .....	47
4.1.3 Target Location (15,8) .....	49
4.1.4 Target Locations (2,8) and (5,10) .....	50
4.1.5 Target Locations (2,10) and (15,12) .....	52
4.1.6 Target Locations (11,4) and (11,14) .....	55
4.2 Performance Metric Results .....	57
4.2.1 Image MSE Results .....	57
4.2.2 Dispersion Results .....	58
4.2.3 Target Location RMSE Results .....	60
4.2.4 Execution Time Results .....	61
4.3 Performance Metric Average Results .....	62
V. Conclusions .....	65
5.1 Future Work .....	67
Bibliography .....	68

## List of Figures

Figure		Page
1.	Illustration of RTI WSN. ....	6
2.	Example of the LOS path for a single obstructed RF link. ....	7
3.	Image of a single NeSh model weighted link. ....	11
4.	Image of a single IAEM weighted link. ....	13
5.	Image of a single link's change in RSS for the ER model. ....	15
6.	Image of a single weighting-g model weighted link. ....	16
7.	NeSh model and Tikhonov regularization attenuation images for $\alpha$ values of 10 (a), 100 (b), 1,000 (c), and 10,000 (d). ....	35
8.	Weighting-g model and Tikhonov regularization attenuation images for $\alpha$ values of 10 (a), 100 (b), 1,000 (c), and 10,000 (d). ....	36
9.	Images of NeSh model weighted links for $\lambda$ values of 0.005 (top), 0.01 (middle), and 0.02 (bottom) for an example link. ....	38
10.	Images of weighting-g model weighted links for $\lambda$ values of 0.025 (top), 0.05 (middle), and 0.10 (bottom) for an example link. ....	39
11.	True attenuation image for target locations (2,8) and (5,10). ....	41
12.	Attenuation image for true target location (9,14) with $k = 10$ estimated target locations (left) and attenuation image for true target locations (2,8) and (5,10) with $k = 10$ estimated target locations (right). ....	43
13.	Attenuation images for target location (9,14). ....	45
14.	Magnified attenuation images for target location (9,14). ....	46
15.	Attenuation images for target location (5,5). ....	47
16.	Magnified attenuation images for target location (5,5). ....	48

Figure	Page
17. Attenuation images for target location (15,8). . . . .	49
18. Magnified attenuation images for target location (15,8). . . . .	50
19. Attenuation images for target locations (2,8) and (5,10). . . . .	51
20. Magnified attenuation images for target locations (2,8) and (5,10). . . . .	52
21. Attenuation images for target locations (2,10) and (15,12). . . . .	53
22. Magnified attenuation images for target location (2,10). . . . .	54
23. Attenuation images for target locations (11,4) and (11,14). . . . .	55
24. Magnified attenuation images for target locations (11,4) and (11,14). . . . .	56
25. Graph of average image MSE results. . . . .	62
26. Graph of true dispersion, average dispersion, and average dispersion error results. . . . .	63
27. Graph of average target location RMSE results. . . . .	63
28. Graph of average execution time results. . . . .	64

## List of Tables

Table		Page
1.	Image MSE Results .....	58
2.	Dispersion Results (ft). True dispersion is 0.93 ft for all true targets. ....	58
3.	Dispersion Error Results (ft) .....	59
4.	Target Location RMSE Results (ft) .....	60
5.	Execution Time Results (seconds).....	61

# MITIGATING THE MULTIPATH EFFECTS ON RADIO TOMOGRAPHIC IMAGING

## I. Introduction

This chapter provides background information about the research topic and problem this thesis will address. It also describes the research objectives that drive the work performed in this thesis. The chapter concludes with a document overview to summarize the next chapters to come.

### 1.1 Problem Background

Radio tomographic imaging (RTI) is a technology used to generate images of the attenuation caused by objects or targets obstructing a wireless sensor network (WSN). As the sensors in the WSN transmit and receive signals, the received signal strengths (RSS) are recorded and used to determine any changes in attenuation [1]. The RTI system utilizes radio waves to transmit signals within the WSN. Multipath propagation is an inherent characteristic of a radio frequency (RF) sensing network [2]. The multipath propagation is also referred to as multipath interference and is an issue because its effects can degrade RTI system performance.

#### 1.1.1 Multipath Interference

Multipath components such as electronic noise, reflection, and shadowing contribute to multipath interference [3, 4, 5]. Electronic noise is attributed to changes in RSS measurements when no targets are present in the WSN. Reflection of the signal

occurs when a target is in close proximity to the line-of-sight (LOS) path of the signal. Shadowing refers to a target obstructing the LOS path of a transceiver pair [5].

Multipath interference introduces imaging artifacts into RTI attenuation images. The imaging artifacts are excess areas of attenuation that can be mistaken for target-induced attenuation and form pseudo-targets. The attenuation introduced by imaging artifacts can degrade the overall RTI system performance by impacting the image and target localization accuracy. Therefore, it is necessary to mitigate the effects of multipath interference in order to yield the best RTI system performance [2].

### **1.1.2 RTI Models and Reconstruction Methods**

RTI models and reconstruction methods work to mitigate multipath interference in different ways. The RTI models consider the changes in RSS measurements caused by target appearance and different multipath components and characterize the target-induced attenuation and multipath interference. The RTI reconstruction methods utilize the RTI models and change in RSS measurements to reconstruct the target-induced attenuation in the form of attenuation images [2]. The attenuation images can then be analyzed to determine image and target localization accuracy. Different RTI reconstruction methods also have unique conditions they set to mitigate multipath interference and suppress imaging artifacts. RTI models and reconstruction methods have unique approaches to mitigating multipath interference and these approaches are strengthened when implemented together.

## **1.2 Research Objectives**

Preliminary research revealed there were novel RTI models and reconstruction methods able to mitigate multipath interference that had not been implemented together yet. Based on the preliminary research, the objectives of this thesis will be to

implement new combinations of RTI models and reconstruction methods and conduct a comparative analysis of how well they perform. Each model will be implemented in conjunction with each reconstruction method to produce different combinations that are capable of mitigating multipath interference in different ways than previously researched.

A comparative analysis will be conducted using qualitative and quantitative assessments. After implementing the combinations in MATLAB and generating the attenuation images, the image data will be used in a target localization algorithm to estimate the target locations. Visual inspection will be used to assess the noise prevalence and target localization accuracy of the images on a qualitative basis. The image accuracy, target localization accuracy, and execution time of the combinations will be assessed by using quantitative performance metrics. The quantitative performance results will ultimately be used to generate ratings for the combinations and these ratings will be compared to determine which combination has the optimum performance.

### **1.3 Document Overview**

This thesis is comprised of five total chapters. Chapter I is a brief overview of the research topic, problem background, and research objectives. Chapter II is a detailed literature review that provides information on the RTI system, models, reconstruction methods, and target localization algorithms. Chapter III discusses the methodology used to carry out the research objectives previously mentioned. Chapter IV presents the subsequent results after executing the methodology in the previous chapter. Chapter V is a summary of the final performance results and ratings that determine which RTI model and reconstruction method combination has the optimal performance.

## II. Background and Literature Review

This chapter provides an overview of existing work pertaining to the RTI system, models, reconstruction methods, and target localization algorithms. The information about the RTI system provides insight as to how the system itself operates. The information about the models provides insight as to how the targets are modeled in a WSN environment and the information about the reconstruction methods provides insight as to how the attenuation images are generated. Lastly, the information on the target localization algorithms discusses different methods for estimating single and multi-target locations.

### 2.1 Radio Tomographic Imaging

Radio tomographic imaging is a device-free localization (DFL) technology that generates images of the attenuation caused by targets obstructing the WSN. The RTI system utilizes RF transmission to pass signals between the transceivers that make up the WSN. The RSS measurements are recorded and used to determine the target-induced attenuation [1].

RF transmission allows the RTI system to transmit signals through mediums such as walls, trees, and smoke while optical and infrared imaging technologies cannot [1, 6]. Also, RF transmission allows the RTI system to effectively operate in darkness where video cameras fail. One disadvantage of RF transmission is significant non-line of sight (NLOS) propagation present in the RSS measurements [1]. It is difficult for the RTI system to distinguish between attenuation caused by a target on the LOS path or NLOS path [7].

RTI has proven useful in scenarios that require low cost, device-free localization and tracking. Most wireless commercial-off-the-shelf (COTS) devices have readily

available RSS measurements which permit the RTI system to operate on the existing network [8]. Also, to perform successful device-free localization and tracking, the target in the WSN does not need a wireless device attached. For these reasons, RTI has been successfully used in the following scenarios: through-wall target monitoring [6, 9], residential monitoring [10, 11], and roadside surveillance [12].

### 2.1.1 Wireless Sensor Network

A wireless sensor network is comprised of transceivers that act as sensors arranged around a defined perimeter. These transceivers are also referred to as nodes. Links are formed between pairs of nodes and the total number of unique two-way links is given by

$$M = \frac{K^2 - K}{2} \quad (1)$$

where  $K$  is the number of nodes in the WSN [1].

The nodes in the WSN communicate via a token passing protocol. Each node transmits a signal to the base station as well as to all of the other nodes [4, 13, 14]. This allows the RSS measurements to be recorded. After the first node transmits a signal, the token is passed to the next sequential node. If the next sequential node does not transmit within the allotted time, the base station passes the token to the next node and the process continues until all of the nodes have had the opportunity to transmit [4, 13, 14].

Targets in the WSN environment absorb, reflect, diffract, or scatter a portion of the transmitted signal power and the signal becomes shadowed. This leads to attenuation which is the reduction of signal amplitude. The attenuation can then be used to determine the locations of the targets because the node locations are known and the attenuation occurs across the node links [1].

Figure 1 depicts an example of the RTI WSN. The nodes are arranged around

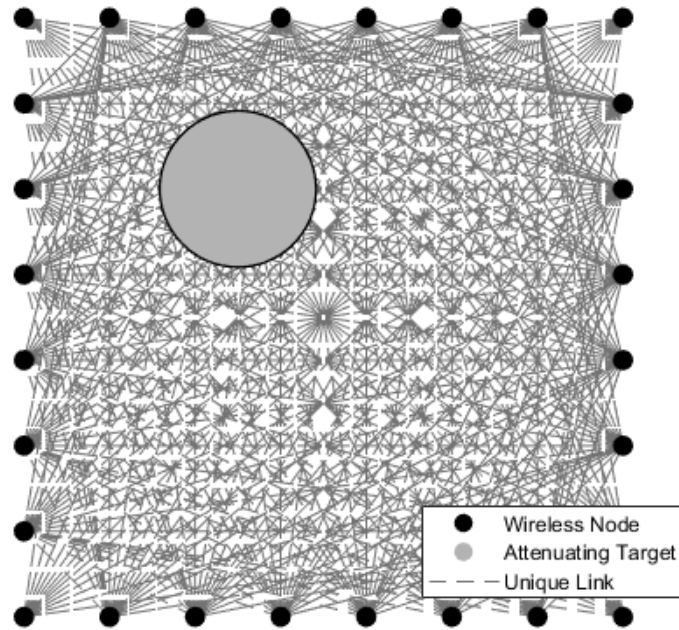


Figure 1: Illustration of RTI WSN.

a defined perimeter and links are created when each individual node is paired with all of the other nodes. When a grid is laid over the RTI WSN, this creates  $N$  pixels with unique locations. Figure 2 illustrates an example of the unique pixel locations and the LOS path which is the most direct path a signal travels from one transceiver to another. On the grid, the direct LOS path is represented by the pixels the RF link directly passes through. The mathematical model for the LOS path uses the ellipse to simplify which pixels lie along the LOS path [1]. In figure 2, the gray target obstructing the link is shown to affect all the yellow pixels that lie within the red ellipse and that affect is known as target-induced attenuation. The blue pixels in the figure are unaffected by the attenuating target and represent the NLOS paths which are indirect paths a signal may travel due to RF multipath signal propagation.

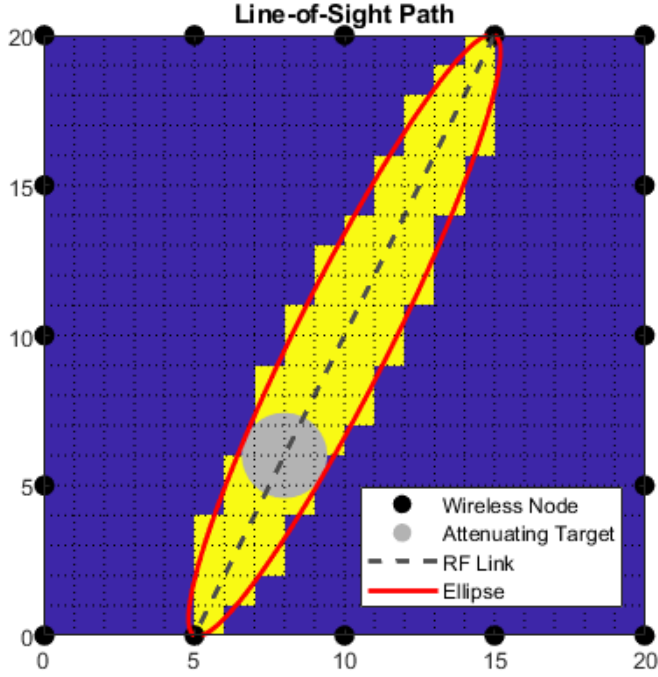


Figure 2: Example of the LOS path for a single obstructed RF link.

### 2.1.2 Linear Formulation

RSS measurements are essential to determining the amount of attenuation that occurs across pixels that make up specific links. The RSS  $y$  of a particular link  $i$  at time  $t$  is given by

$$y_i(t) = P_i - L_i - S_i(t) - F_i(t) - v_i(t) \quad (2)$$

where

- $P_i$  is transmitted power
- $L_i$  is static loss due to distance, antenna patterns, etc.
- $S_i(t)$  is shadowing loss due to the attenuating target(s)
- $F_i(t)$  is fading loss due to constructive or destructive interference in multipath environments

- $v_i(t)$  is measurement noise.

All of the above variables are measured in decibels [1]. The shadowing loss variable  $S_i(t)$  is of particular interest because it is approximately equal to the sum of attenuation in each pixel along a link. For each link, the pixels affect the amount of attenuation differently and therefore a weighting is applied. For one specific link, the shadowing loss is represented by

$$S_i(t) = \sum_{j=1}^N w_{ij} x_j(t) \quad (3)$$

where  $w_{ij}$  is the weight of pixel  $j$  on link  $i$  and  $x_j(t)$  is the attenuation in pixel  $j$  at time  $t$  [1].

A calibration step must be performed in order to calculate the change in RSS  $\Delta y_i$ . The calibration step is performed by first recording the RSS measurements when there are no targets obstructing the links in the WSN [15]. The calibration RSS measurements  $y_i(t_c)$  are then subtracted from the RSS measurements recorded when there are targets obstructing the links  $y_i(t)$  [1, 2, 16]. Under the assumption that static losses become negligible over time, the change in RSS becomes [1]

$$\begin{aligned} \Delta y_i &= y_i(t) - y_i(t_c) \\ &= S_i(t) - S_i(t_c) + F_i(t) - F_i(t_c) + v_i(t) - v_i(t_c). \end{aligned} \quad (4)$$

The fading loss  $F_i(t)$  and measurement noise  $v_i(t)$  can be combined into the noise term  $n_i$  given by [1]

$$n_i = F_i(t) - F_i(t_c) + v_i(t) - v_i(t_c). \quad (5)$$

Equations (3) and (5) can then be substituted into equation (4) to generate the

following formula for change in RSS

$$\Delta y_i = \sum_{j=1}^N w_{ij} \Delta x_j + n_i \quad (6)$$

where  $\Delta x_j$  is the change in attenuation for pixel  $j$  from times  $t_c$  to  $t$  [1]. When all of the links are considered at once, equation (6) can be written in matrix form as

$$\Delta \mathbf{y} = \mathbf{W} \Delta \mathbf{x} + \mathbf{n} \quad (7)$$

where  $\Delta \mathbf{y}$  is the length  $M$  change in RSS vector,  $\mathbf{W}$  is the  $M \times N$  weight matrix whose rows contain the weights of the pixels for the node links and whose columns represent the individual pixels,  $\Delta \mathbf{x}$  is the length  $N$  attenuation image vector to be estimated, and  $\mathbf{n}$  is the length  $M$  noise vector [1]. To shorten the notation in equation (7), the terms  $\mathbf{x}$  and  $\mathbf{y}$  will replace  $\Delta \mathbf{x}$  and  $\Delta \mathbf{y}$ .

### 2.1.3 Noise

According to [1], the noise vector in equation (7) is attributed to RSS time variation when no targets are obstructing the LOS paths. In the absence of any target, the RSS measurements should be constant over time, but this is not the case due to residual noise in the system. Also, multipath interference contributes to the noise in the RTI system because it effects the NLOS paths [17].

Patwari and Wilson collected experimental noise samples by implementing the RTI system and recording the RSS measurements of links when no targets were present in the environment. For a given link, the results showed periods of heavy fading and low fading which corresponded to a combination of high variance and low variance Gaussian distributions. The mean data from each link was extracted and fitted with a Gaussian mixture distribution that provided a sufficient approximation [1]. Most

commonly in RTI research, the noise is modeled as a zero-mean Gaussian distribution known as additive white Gaussian noise (AWGN) [18, 17, 19, 20]. The AWGN model and Gaussian mixture model both fit the data in a similar fashion [1].

## 2.2 RTI Models

RTI models mainly consider how the RSS measurements for each link vary based on the target’s location and geometry. Some models further take into account the multipath components that are introduced by electronic noise, reflection, and shadowing. The purpose of the models is to characterize RSS attenuation and multipath interference in order to produce attenuation images that have the least amount of artifacts [2].

### 2.2.1 Network Shadowing Model

Wilson and Patwari introduced the network shadowing (NeSh) model as part of the RTI method for model-based DFL [21, 22]. The weight matrix  $\mathbf{W}$  is used in the NeSh model to determine the pixel weights necessary to calculate the change in RSS  $\mathbf{y}$ . According to [19], the weight matrix can be represented as

$$\mathbf{W} = \mathbf{S} \odot \mathbf{\Omega} \tag{8}$$

where  $\mathbf{S}$  is the binary selection matrix,  $\mathbf{\Omega}$  is a matrix that contains the real-valued weight magnitudes, and  $\odot$  signifies element-wise multiplication.

The NeSh model utilizes an ellipse with foci at each node to determine the weight-

ing of each pixel for a particular link. The pixel weight is calculated by

$$w_{ij} = \frac{1}{\sqrt{d_i}} \begin{cases} 1, & \text{if } d_{ij}(1) + d_{ij}(2) < d_i + \lambda \\ 0, & \text{otherwise} \end{cases} \quad (9)$$

where  $d_i$  is the distance between the two nodes that make up link  $i$ ,  $d_{ij}(1)$  and  $d_{ij}(2)$  are the distances from the center of pixel  $j$  to the nodes of link  $i$ , and  $\lambda$  is the width of the ellipse [1]. The width of the ellipse is generally set low to simulate the LOS path, however it is ultimately tuned based on user specification. Figure 3 illustrates that only pixels that fall within the bounds of the ellipse for a particular link have a nonzero weight [1].

The length of the node link has an impact on the change in RSS. Longer links that are obstructed by targets have less change in RSS because the signals have a longer

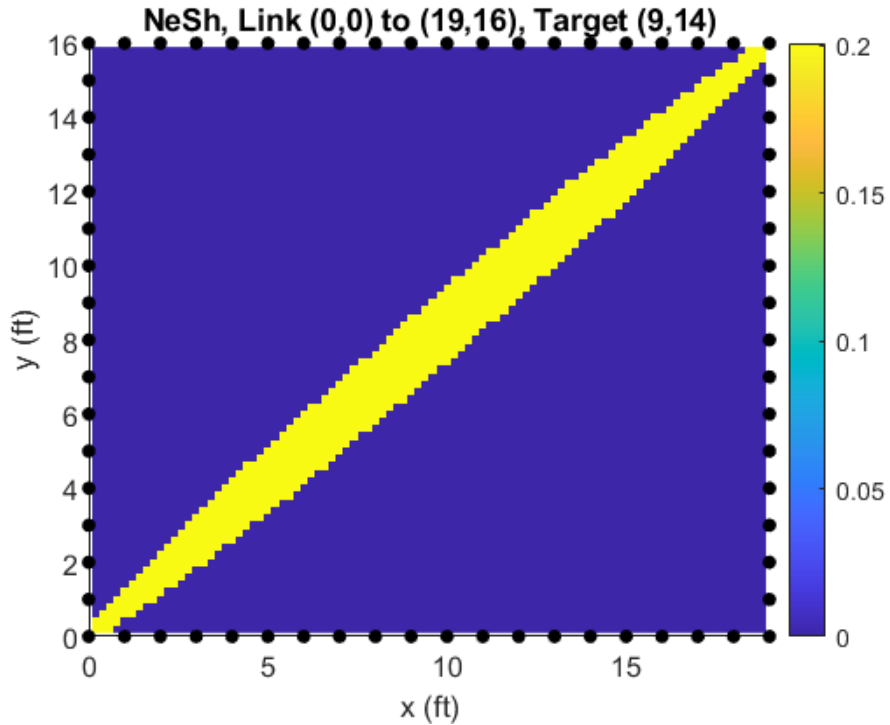


Figure 3: Image of a single NeSh model weighted link.

distance to travel and can reflect around the targets, whereas the shorter obstructed links exhibit substantial change in RSS due to the abrupt target interference [1]. In equation (9), the weights of the pixels that fall within the ellipse are equal to the inverse square root of the distance of link  $i$ . This is consistent with the knowledge that the change in RSS is inversely proportional to link length [16]. Although the NeSh model considers the length of the links, it does not consider the distance between the targets and links. The model also gives equal weights to all of the pixels that fall within the ellipse, however this is inconsistent with the fact that the targets affect pixel locations differently. Research has shown that targets have a greater influence on nodes when they are located closer to them [22]. For these reasons, the NeSh model is not the most practical for operational applications.

### 2.2.2 Inverse Area Elliptical Model

The goal of the inverse area elliptical model (IAEM) is to relate signal shadowing to attenuation occurring at specific locations in the WSN. The IAEM achieves this goal by accounting for the fact that some areas of the ellipse contribute more to the change in RSS than others. To demonstrate the contributions, the weight matrix is set equal to the inverse area of the smallest ellipse containing a particular link [20]. The area of the ellipse is given by

$$A(d_i, \lambda_{ij}) \approx \frac{\pi}{4} d_i \sqrt{2d_i \lambda_{ij}} \quad (10)$$

where  $d_i$  is the distance between the two nodes that make up link  $i$  and  $\lambda_{ij}$  is the width of the ellipse that is either a set tunable parameter or given by

$$\lambda_{ij} = d_{ij}(1) + d_{ij}(2) - d_i \quad (11)$$

where  $d_{ij}(1)$  and  $d_{ij}(2)$  are the distances from the center of pixel  $j$  to the nodes of link  $i$  [19]. Equations (10) and (11) are used to calculate the IAEM given by

$$\mathbf{W} = \begin{cases} A^{-1}(d_i, \lambda_{min}), & \text{if } \lambda_{ij} < \lambda_{min} \\ A^{-1}(d_i, \lambda_{ij}), & \text{if } \lambda_{ij} \geq \lambda_{min} \end{cases} \quad (12)$$

where  $\lambda_{min}$  is a tunable parameter [19]. The weights are bounded by the semi-minor axis lengths determined by  $\lambda_{min}$  and  $\lambda_{ij}$  [20]. Figure 4 is an example of one IAEM weighted link.

The IAEM utilizes the ellipse because the Fresnel zone is known to have an ellipsoidal shape. Although the NeSh model also utilizes the ellipse, the IAEM considers the fact that the change in RSS is different for signals that travel close to the edge of the ellipse as opposed to those traveling near the LOS path. The signals traveling

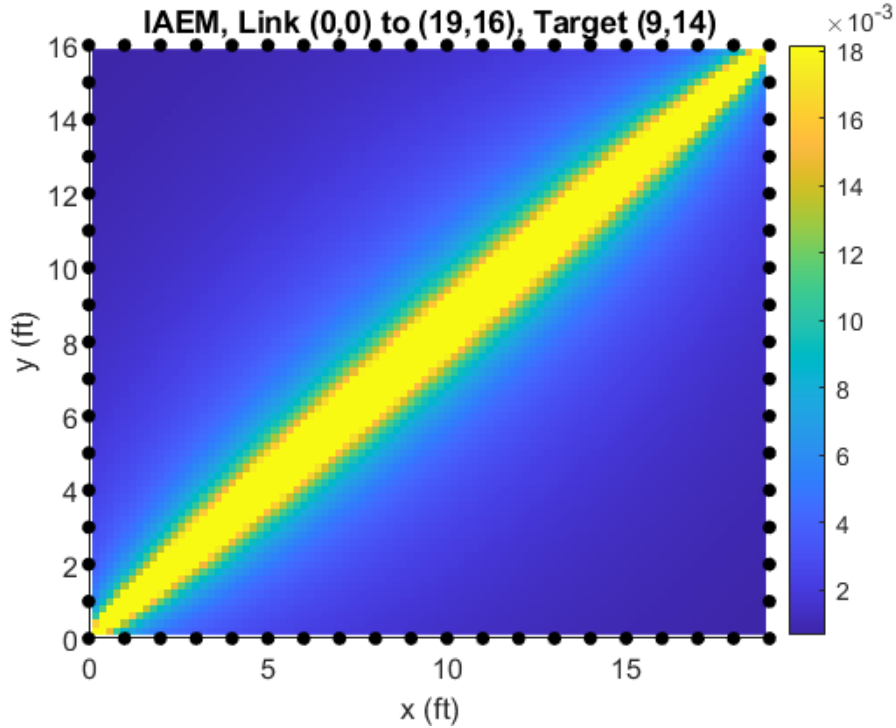


Figure 4: Image of a single IAEM weighted link.

along the edge of the ellipse have a farther distance to travel and therefore have less impact on change in RSS. For this reason, the IAEM weights pixels farther from the LOS path less than those closer to the LOS path [20]. This is a substantial improvement, however the contributions of the individual pixels within an ellipse cannot be distinguished [16].

### 2.2.3 Exponential-Rayleigh Model

The Exponential-Rayleigh (ER) model characterizes the change in RSS while also addressing multipath interference which degrades DFL accuracy. The ER model consists of a large-scale exponential component that represents the link shadowing and a Rayleigh component that represents the multipath interference introduced by targets obstructing the links [18]. For a single target, the ER attenuation model is expressed as

$$y_i(\mathbf{k}) = \beta_a e^{\frac{-\lambda_i(\mathbf{k})}{\sigma_a}} - \beta_b \lambda_i(\mathbf{k}) e^{\frac{-\lambda_i^2(k)}{\sigma_b}} \quad (13)$$

where  $i$  is the particular link,  $\mathbf{k}$  is the length  $M$  vector of estimated target locations,  $\beta_a$  and  $\sigma_a$  are the attenuation parameters,  $\beta_b$  and  $\sigma_b$  are the model parameters, and  $\lambda_i$  is the excess path length which is the difference between the major axis length of the ellipse and the intra-focal distance as in equation (11) [18, 19]. Figure 5 illustrates an example of the change in RSS for one link. The pixel intensities greater than zero indicate target-induced attenuation and the pixel intensities less than zero imply RSS enhancement [18]. For multiple targets, the ER attenuation model is expressed as

$$y(\mathbf{K}) = \sum_{g=1}^G y_i(\mathbf{k}, g) \quad (14)$$

where  $G$  is the total number of targets and  $y_i(\mathbf{k}, g)$  is the ER component of target  $g$  [18].

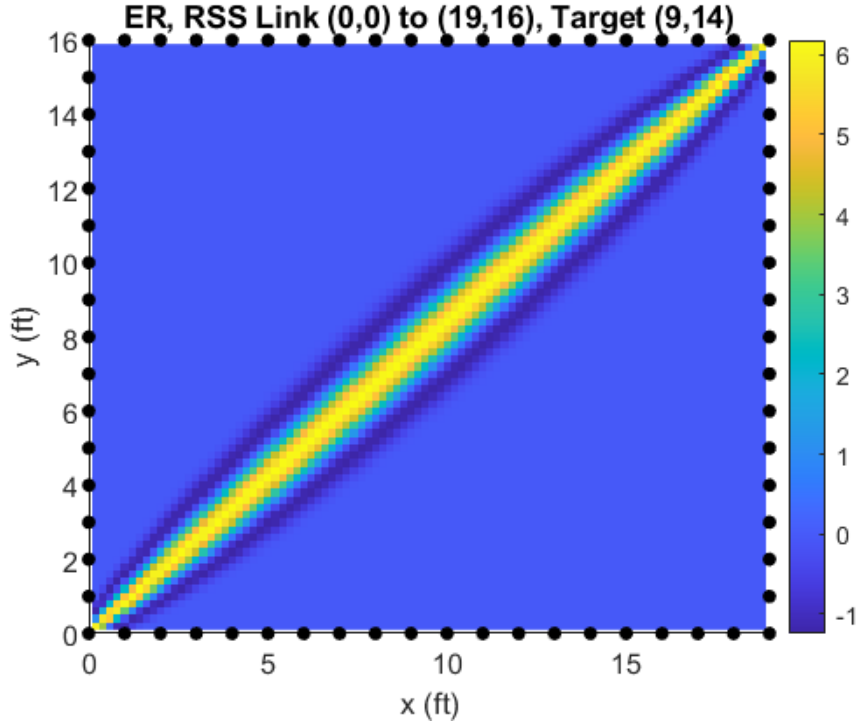


Figure 5: Image of a single link’s change in RSS for the ER model.

For equation (14), the expectation maximization (EM) algorithm is used to determine the attenuation parameters ( $\beta_a$  and  $\sigma_a$ ) and the model parameters ( $\beta_b$  and  $\sigma_b$ ). Although the ER model enhances the multipath components to account for their effect on the change in RSS, this requires the use of the EM algorithm which adds computational complexity [18]. Conversely, the NeSh model and IAEM more simply rely on the weight matrix calculations to characterize the changes in attenuation.

In [18], the ER model is not used to create images of the attenuation. Instead, equations (13) and (14) are used in conjunction with particle filtering to estimate a known number of target locations. This thesis will focus on the RTI models that are implemented in conjunction with reconstruction methods to generate attenuation images and estimate target localization from those images.

### 2.2.4 Weighting-g Model

The weighting-g model is an elliptical model that determines the weight matrix based on the distance of the pixels in the ellipse and their proximity to the LOS path [16]. The model introduces a distance attenuation factor that improves target localization performance. The weighting-g model is represented by

$$w_{ij} = \begin{cases} e^{-h}, & \text{if } d_{ij}(1)+d_{ij}(2) < d_i + \lambda \\ 0, & \text{otherwise} \end{cases} \quad (15)$$

where  $h$  is the distance between each pixel inside the ellipse and the LOS path,  $d_{ij}(1)$  and  $d_{ij}(2)$  are the distances from the center of pixel  $j$  to the nodes of link  $i$ ,  $d_i$  is the distance between the two nodes that make up link  $i$ , and  $\lambda$  is the tunable width of the ellipse [16]. Figure 6 illustrates an example of one weighted link.

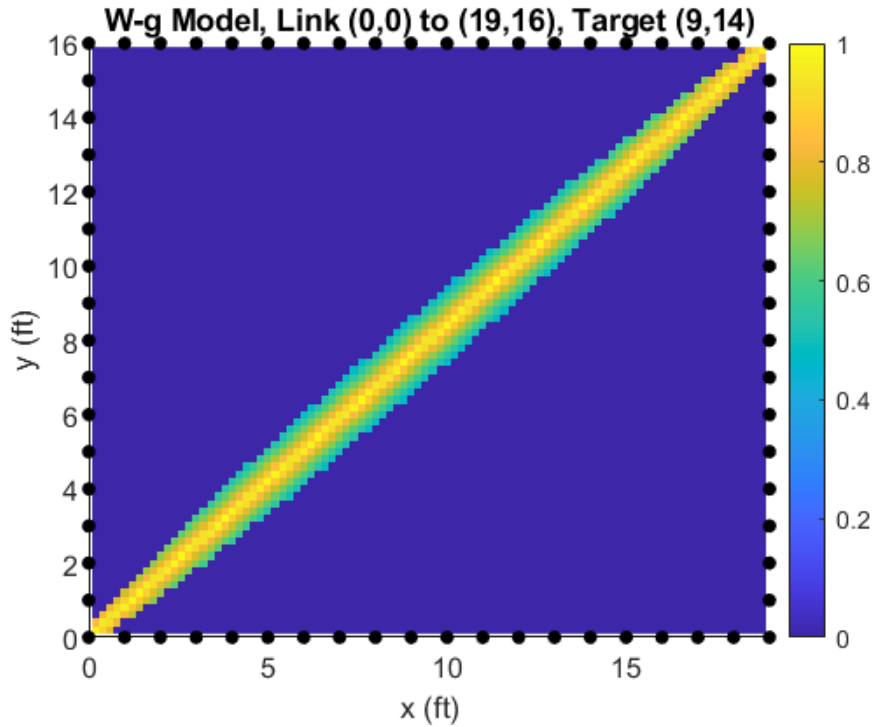


Figure 6: Image of a single weighting-g model weighted link.

The signal shadowing along LOS paths is greater than the shadowing along NLOS paths [16, 23]. The weighting-g model addresses this difference in shadowing by assigning different weights to the pixels within the ellipse that reside along the LOS path or NLOS path. In equation (15), pixels that fall within the ellipse are given a magnitude equal to the distance attenuation factor  $e^{-h}$ . This factor is different for every pixel due to the fact that every pixel has a unique location. The factor also ensures the pixels that contain the LOS paths have greater weights than the pixels that contain the NLOS paths. This is consistent with the shadowing behavior that occurs in a real world environment [16].

The weighting-g model differs from the previously described RTI models. Unlike the NeSh model, the weighting-g model considers the distance relationship between the pixels and LOS path and attributes different weights to the pixels which is more consistent with actual shadowing behavior. The IAEM model demonstrates actual shadowing behavior, however the individual pixels are not all uniquely distinguished [16]. Also, the weighting-g model resists multipath interference by utilizing the distance attenuation factor to condense the number of pixels that have significant attenuation and reduce the appearance of pseudo targets in the attenuation image [16]. The ER model also addresses multipath interference, but it is more computationally complex because it implements the EM algorithm [18].

### 2.3 RTI Reconstruction Methods

RTI reconstruction methods are responsible for generating the estimated attenuation images used to approximate the locations of targets in the WSN environment. These methods rely on the change in RSS data characterized by the RTI models in section 2.2 [2]. RTI reconstruction is an ill-posed inverse problem meaning that a small amount of noise can be substantially amplified. This noise amplification can

then degrade the attenuation image quality and render inaccurate target localization. For these reasons, the reconstruction methods must account for the presence of noise which introduces artifacts into the attenuation images [2].

### 2.3.1 Tikhonov Regularization

To implement Tikhonov regularization, a derivative energy term is added to the least squares solution. The least squares solution minimizes the fit error in equation (7) by manipulating the least-squared error given by

$$\mathbf{x}_{LS} = \arg \min_x \|\mathbf{W}\mathbf{x} - \mathbf{y}\|_2^2 \quad (16)$$

where  $\mathbf{W}$  is the length  $M \times N$  weight matrix,  $\mathbf{x}$  is the length  $N$  attenuation image vector, and  $\mathbf{y}$  is the length  $M$  change in RSS vector [1]. The least squares solution takes the gradient of equation (16) and sets it equal to zero to yield

$$\mathbf{x}_{LS} = (\mathbf{W}^T \mathbf{W})^{-1} \mathbf{W}^T \mathbf{y}. \quad (17)$$

However, this solution is only valid if  $\mathbf{W}$  is full rank and this is not true in RTI systems due to the ill-posed inverse problem. Therefore, regularization is used to introduce information into the model that will tackle the ill-posed issue [1].

Tikhonov regularization is represented by

$$f(x) = \frac{1}{2} \|\mathbf{W}\mathbf{x} - \mathbf{y}\|_2^2 + \alpha \|\mathbf{Q}\mathbf{x}\|_2^2 \quad (18)$$

where  $\alpha$  is an adjustable regularization parameter and  $\mathbf{Q}$  is the Tikhonov matrix that approximates the derivative operator [1]. By substituting in the difference matrices

for  $\mathbf{Q}$ , equation (18) becomes

$$f(x) = \frac{1}{2} \|\mathbf{W}\mathbf{x} - \mathbf{y}\|^2 + \alpha(\|\mathbf{D}_x\mathbf{x}\|^2 + \|\mathbf{D}_y\mathbf{y}\|^2) \quad (19)$$

where  $\mathbf{D}_x$  and  $\mathbf{D}_y$  are the difference operators in the horizontal and vertical directions respectively [1]. After taking the gradient of equation (19) and setting it equal to zero, the estimated attenuation becomes

$$\hat{\mathbf{x}} = (\mathbf{W}^T\mathbf{W} + \alpha(\mathbf{D}_x^T\mathbf{D}_x + \mathbf{D}_y^T\mathbf{D}_y))^{-1}\mathbf{W}^T\mathbf{y}. \quad (20)$$

The estimated attenuation can now be represented as a linear transformation of the change in RSS data given by

$$\hat{\mathbf{x}} = \mathbf{\Pi}\mathbf{y} \quad (21)$$

where  $\mathbf{\Pi}$  is given by

$$\mathbf{\Pi} = (\mathbf{W}^T\mathbf{W} + \alpha(\mathbf{D}_x^T\mathbf{D}_x + \mathbf{D}_y^T\mathbf{D}_y))^{-1}\mathbf{W}^T. \quad (22)$$

The computational simplicity of the linear transformation is one of the main benefits of Tikhonov regularization. Also, the linear transformation allows for faster reconstruction because it does not rely on instantaneous measurements and  $\mathbf{\Pi}$  can be precalculated [1]. Tikhonov regularization successfully minimizes noise energy and generates smooth attenuation images, however some of the target-induced attenuation may be eliminated throughout the process [2].

### 2.3.2 Heterogeneous Bayesian Compressive Sensing

Heterogeneous Bayesian compressive sensing (HBCS) is a type of BCS that developed from sparse Bayesian learning (SBL) [23]. BCS implements the Bayesian

method which recognizes all unknown variables as random variables that follow certain probability distributions [17, 24, 25]. SBL is a machine learning tool that can be successfully applied to the RTI system because the attenuation image has a sparse number of pixels that account for the target-induced attenuation [17]. HBCS solves sparse signal recovery by implementing a heterogeneous noise variance learning algorithm to estimate the attenuation image [23].

The HBCS method applies a zero-mean multivariate Gaussian distribution over the attenuation image  $\mathbf{x}$  and heterogeneous noise  $\mathbf{n}$ . The Bayesian rule is then applied to determine the posterior distribution

$$\begin{aligned} p(\mathbf{x}|\mathbf{y}, \boldsymbol{\alpha}, \boldsymbol{\beta}) &= \frac{p(\mathbf{y}|\mathbf{x}, \boldsymbol{\beta})p(\mathbf{x}|\boldsymbol{\alpha})}{\int p(\mathbf{y}|\mathbf{x}, \boldsymbol{\beta})p(\mathbf{x}|\boldsymbol{\alpha})d\mathbf{x}} \\ &= \mathcal{N}(\boldsymbol{\mu}, \boldsymbol{\Sigma}) \end{aligned} \quad (23)$$

where  $\mathbf{x}$  is the length  $N$  attenuation image vector,  $\mathbf{y}$  is the length  $M$  change in RSS vector,  $\boldsymbol{\alpha}$  is the length  $N$  vector  $[\alpha_1, \alpha_2, \dots, \alpha_N]^T$  whose inverse makes up the attenuation covariance when placed on a matrix diagonal, and  $\boldsymbol{\beta}$  is the length  $M$  vector  $[\beta_1^{-2}, \beta_2^{-2}, \dots, \beta_M^{-2}]^T$  whose inverse makes up the noise covariance when placed on a matrix diagonal [17, 23]. Modeling the noise in a heterogeneous fashion is more similar to noise in a real world environment because the noise levels vary for different links [23]. The mean  $\boldsymbol{\mu}$  of the posterior Gaussian distribution is given by

$$\boldsymbol{\mu} = \boldsymbol{\Sigma}\mathbf{W}^T\mathbf{B}\mathbf{y} \quad (24)$$

where  $\mathbf{W}$  is the weight matrix and  $\mathbf{B}$  is the diagonal entries of  $\boldsymbol{\beta}$  [23]. The covariance  $\boldsymbol{\Sigma}$  is given by

$$\boldsymbol{\Sigma} = [\mathbf{W}^T\mathbf{B}\mathbf{W} + \mathbf{A}]^{-1} \quad (25)$$

where  $\mathbf{A}$  is the diagonal entries of  $\boldsymbol{\alpha}$  [23]. Using the Gaussian posterior distribution

in equation (23), the attenuation image is estimated by the following maximum a posterior (MAP) solution,

$$\mathbf{x}_{HBCS} = \arg \max_x p(\mathbf{x}|\mathbf{y}, \boldsymbol{\alpha}, \boldsymbol{\beta}). \quad (26)$$

Equation (26) can be further represented by

$$\mathbf{x}_{HBCS} = [\mathbf{W}^T \mathbf{B} \mathbf{W} + \mathbf{A}]^{-1} \mathbf{W}^T \mathbf{B} \mathbf{y}. \quad (27)$$

To successfully conduct sparse signal recovery,  $\boldsymbol{\alpha}$  and  $\boldsymbol{\beta}$  must be properly estimated. These parameters are estimated using a maximum likelihood solution implemented in the heterogeneous noise variance learning algorithm. The algorithm uses the parameters  $\boldsymbol{\mu}$  and  $\boldsymbol{\Sigma}$  to update  $\boldsymbol{\alpha}$  and  $\boldsymbol{\beta}$ , the  $\boldsymbol{\alpha}$  and corresponding  $\mathbf{W}$  values are pruned, the corresponding pixel in  $\mathbf{x}$  is set to 0 when  $\alpha_i$  is larger than a threshold value, and the process continues until  $\boldsymbol{\mu}$  converges [23]. In HBCS, the noise variance terms provide more degrees of freedom to maximize sparse solutions. By this account, HBCS outperforms BCS [23]. However, the algorithmic updates for  $\boldsymbol{\beta}$  render the algorithm used in HBCS computationally complex [23]. Also, if the multipath interference that contributes to noise in the environment is sparse, this could lead to decreased target localization accuracy [2].

### 2.3.3 Feedback-Based Sparse Bayesian Learning

Feedback-based sparse Bayesian learning implements fast SBL for both heterogeneous and homogeneous noise scenarios. It can be applied to the RTI system because the attenuation image is considered sparse. The feedback-based SBL outperforms fast SBL because the inaccurate noise estimation of fast SBL reduces the reconstruction image quality [17].

To improve image reconstruction quality, feedback-based SBL implements energy feedback from signal space to noise space. In this way, the noise estimation is linked to signal estimation. This is accomplished by modeling the noise as a 3-layer framework of one zero-mean Gaussian distribution and two Gamma distributions [17]. The distributions are defined as

$$p(\mathbf{n}|\boldsymbol{\beta}) = \prod_{i=1}^M \mathcal{N}(n_i|0, \beta_i^{-1}) \quad (28)$$

$$p(\boldsymbol{\beta}|\boldsymbol{\varepsilon}) = \prod_{i=1}^M \Gamma(\beta_i|1, s_i \cdot \varepsilon_i) \quad (29)$$

$$p(\boldsymbol{\varepsilon}|\vartheta) = \prod_{i=1}^M \Gamma(\varepsilon_i|\vartheta, \vartheta) \quad (30)$$

where  $\mathbf{n}$  is the length  $M$  noise vector,  $\boldsymbol{\beta}$  is the length  $M$  reciprocal of noise variance vector,  $\varepsilon_i$  is equal to  $\frac{\vartheta}{s_i \beta_i + \vartheta}$ ,  $\vartheta$  is a user-defined parameter, and  $s_i$  is a factor of the scale-parameter in the Gamma distribution given by

$$s_i = \frac{\bar{P}_x}{\bar{P}_n} \cdot \beta_i \quad (31)$$

where  $\bar{P}_x$  is the mean power of the signal and  $\bar{P}_n$  is the mean power of the noise [17]. Based on equation (31), the signal power has an influence on the noise model in equation (29) [17]. Since feedback-based SBL focuses on a more accurate noise model, the signal  $\mathbf{x}$  remains modeled as a zero-mean Gaussian with covariance  $\boldsymbol{\alpha}^{-1}$  as in HBCS. After applying the Bayesian method, the posterior distribution is the same as equation (23) for HBCS [17].

The fast feedback-based SBL algorithm is implemented to generate the attenuation image. The algorithm works to estimate the hyper-parameters  $\boldsymbol{\alpha}$  and  $\boldsymbol{\beta}$  which are used to update  $\boldsymbol{\mu}$  and  $\boldsymbol{\Sigma}$  and determine whether specific column vectors of  $\mathbf{W}$  are used [17]. Unlike the SBL algorithm, the fast feedback-based SBL algorithm executes

quicker and provides more accurate target localization due to the energy feedback contribution [17].

### 2.3.4 Low-Rank and Sparse Decomposition

Low-rank and sparse decomposition (LRSD) separates the environmental background image from the target-induced foreground image to improve attenuation image quality and target localization accuracy [2]. The image artifacts are reduced by restricting the background environment using a low-rank condition. After constraining the background, the sparse target-induced foreground is enhanced [2]. The sparsity algorithm is then used to obtain a solution for  $\mathbf{x}$ .

The attenuation image  $\mathbf{x}$  can be represented as the combination of the environmental background image  $\mathbf{l}$  and the target-induced foreground image  $\mathbf{s}$  [2, 26, 27]. The combination is given by

$$\mathbf{x} = \mathbf{l} + \mathbf{s}. \quad (32)$$

Equation (32) can also be expressed in matrix form by reshaping the  $\mathbf{l}$  and  $\mathbf{s}$  vectors so they have the same dimensions as the true image. The matrix form is given by

$$\mathbf{X} = \mathbf{L} + \mathbf{S}. \quad (33)$$

In other sparsity-regularized methods such as BCS and HBCS, the imaging artifacts caused by multipath interference may be mistaken as the target-induced attenuation [2]. To mitigate this mistake, the LRSD method uses a sufficient constraint to suppress the artifacts in  $\mathbf{L}$ . LRSD then implements a sparsity-regularized algorithm to recognize the target-induced attenuation in  $\mathbf{S}$  [2].

The LRSD optimization problem is used to solve for the attenuation image. The

optimization problem is given by

$$\mathbf{x} = \arg \min_{\mathbf{l}, \mathbf{s}} \|\mathbf{y} - \mathbf{W}(\mathbf{l} + \mathbf{s})\|_2^2 + \|\mathbf{L}\|_* + \alpha \|\mathbf{S}\|_1 \quad (34)$$

where  $\mathbf{y}$  is the change in RSS vector,  $\mathbf{W}$  is the weight matrix,  $\|\mathbf{L}\|_* = \sum_i \sigma_i(\mathbf{L})$  is the nuclear norm for the minimized rank,  $\sigma_i(\mathbf{L})$  is the  $i^{\text{th}}$  singular value of  $\mathbf{L}$ , and  $\alpha$  is the regularization constant [2]. The background image vector  $\mathbf{l}$  is solved for by using partial singular value decomposition (SVD) in the following formula

$$\begin{aligned} [\mathbf{U}^{[c]}, \mathbf{\Sigma}^{[c]}, \mathbf{V}^{[c]}] &= SVD(\mathbf{Y}^* - \mathbf{S}^{[c]}) \\ \hat{\mathbf{L}}^{[c+1]} &= \mathbf{U}_{:,1:r}^{[c]} \cdot \mathbf{\Sigma}_{1:r,1:r}^{[c]} \cdot \mathbf{V}_{:,1:r}^{[c]T} \\ \hat{\mathbf{l}}^{[c+1]} &= \text{Vec}(\hat{\mathbf{L}}^{[c]}) \end{aligned} \quad (35)$$

where  $c$  is the iteration count,  $\mathbf{U}$  is a  $M \times M$  matrix whose columns form orthonormal vectors,  $\mathbf{V}$  is a  $N \times N$  matrix whose columns form orthonormal vectors,  $\mathbf{Y}^*$  is the matrix form of the reshaped vector  $\mathbf{y}^* = \mathbf{W}^* \mathbf{y}$  according to the notation in [2],  $\mathbf{S}$  is the matrix form of the reshaped vector  $\mathbf{s}$ ,  $\mathbf{\Sigma}$  is a  $M \times N$  matrix whose diagonal entries are the singular values of  $(\mathbf{Y}^* - \mathbf{S}^{[c]})$ , and  $\text{Vec}$  is the vectorization of matrix  $\mathbf{L}$  [2]. The foreground image  $\mathbf{s}$  is estimated by

$$\hat{\mathbf{s}}^{[c+1]} = \arg \min_{\mathbf{s}} \|\mathbf{y} - \mathbf{W}(\hat{\mathbf{l}}^{[c+1]} + \mathbf{s})\|_2^2 + \alpha \|\mathbf{s}\|_1. \quad (36)$$

To solve (36), the iterative shrinkage-thresholding algorithms in [28] are used. The foreground image is then given by

$$\hat{\mathbf{s}}^{[c+1]} = \mathbf{S}_{\alpha\tau} \{\hat{\mathbf{s}}^{[c]} - 2\tau[\mathbf{\Psi}(\hat{\mathbf{l}}^{[c+1]} + \hat{\mathbf{s}}^{[c]}) - \mathbf{y}^*]\} \quad (37)$$

where  $\mathbf{\Psi} = \mathbf{W}^* \mathbf{W}$ ,  $\mathbf{y}^* = \mathbf{W}^* \mathbf{y}$  according to the notation in [2],  $\tau$  is the step size, and

$\mathbf{S}_{\alpha\tau}$  is the soft thresholding operator given by

$$\mathbf{S}_{\alpha\tau}(\mathbf{z})_i = \text{sign}(z_i)\max(0, |z_i| - \alpha\tau) \quad (38)$$

where  $\text{sign}$  is the signum function [2]. After  $\hat{\mathbf{I}}$  and  $\hat{\mathbf{s}}$  converge, the attenuation image  $\hat{\mathbf{x}}$  is obtained by adding  $\hat{\mathbf{I}}$  and  $\hat{\mathbf{s}}$  [2].

Similar to HBCS and feedback-based SBL, LRSD implements a sparsity method to reconstruct the attenuation image [2, 17, 23]. However, HBCS and feedback-based SBL focus on determining the proper distributions to model the multipath interference which is environment dependent [17, 23]. Conversely, LRSD focuses on the suppression of the multipath interference and the enhancement of the target-induced attenuation to reconstruct the attenuation image [2].

## 2.4 Target Localization

After implementing the RTI reconstruction method to generate the attenuation image, the image is analyzed to determine target localization. The algorithm used to perform target localization depends on the number of targets in the environment. Multi-target localization algorithms are capable of estimating one or more target locations, however the same is not true for single target localization algorithms [8].

### 2.4.1 Single Target Localization

For single target scenarios, one method of target localization is finding the center of the highest intensity pixel in  $\mathbf{x}$ . This pixel location is regarded as the estimated target location [16, 17]. The estimated target location is represented by

$$\hat{\mathbf{z}} = [x_k, y_k] \quad (39)$$

where  $k = \arg \max(\mathbf{x})$ ,  $x_k$  is the x-coordinate of the highest intensity pixel, and  $y_k$  is the y-coordinate of the highest intensity pixel [17]. If the brightest pixel in  $\mathbf{x}$  belongs to a pseudo-target introduced by noise, the pseudo-target location will falsely be estimated as the actual target location. Therefore, it is vital to implement the proper model and reconstruction method to reduce the presence of artifacts and potential pseudo targets [16].

## 2.4.2 Multi-Target Localization

Clustering algorithms such as hierarchical agglomerative clustering (HAC) and k-means clustering are used for multi-target localization [8, 18]. Pixel clusters are identified and the centers of the clusters known as centroids are regarded as the estimated target locations [8]. For both methods, a threshold is set in order to reduce the number of pixels that are analyzed as possible target locations [29, 30, 31].

### 2.4.2.1 Hierarchical Agglomerative Clustering

The HAC algorithm can be used to estimate an unknown number of targets. HAC initially considers each pixel a cluster. During each iteration, the two closest clusters are merged together. The average linkage distance between two clusters is calculated by taking the average of the Euclidean distances between all the pixels that make up the clusters. This repeats until the minimum of the average linkage distances is greater than a defined threshold [29]. Low threshold values result in several small clusters while high values result in fewer larger clusters. For each cluster, the pixel with the highest intensity is then selected as the cluster head [29]. To reduce the complexity of target localization, the number of cluster heads is further condensed via a gating process. The gating process entails eliminating cluster heads whose locations fall outside of a defined radius around possible targets and whose pixel

intensities fall below a certain threshold [29]. Lastly, the remaining cluster heads with the highest intensities are regarded as the estimated target locations. Although HAC can be useful in scenarios where the number of targets is unknown, it relies on an experimentally derived threshold value that will vary for targets of different sizes. Therefore, this threshold renders HAC inappropriate to use in real world applications where the threshold cannot be experimentally derived from target data.

### 2.4.2.2 K-Means Clustering

The k-means algorithm works to minimize the average squared distance between points that form a cluster [31]. For the RTI system, the pixel locations selected via thresholding correspond to the points in the k-means algorithm. To execute k-means, the number of clusters  $k$  is required as an input. The number of clusters should be chosen based on the number of targets in the environment. The cluster centers are then chosen uniformly at random from the pixel locations, each pixel is assigned to the closest center, and each center is recalculated as the center of mass of all the pixels that make up its corresponding cluster [31]. The process repeats until the cluster assignments no longer change.

Although the k-means algorithm executes quickly with few iterations, it determines locally optimum target locations that may be inaccurate [30]. The k-means++ algorithm improves the speed and target localization accuracy by choosing random starting centers with specific probabilities [31]. Each new center has a probability that is proportional to the distance from itself to the closest center already chosen. The probability is given by

$$\frac{D(p')^2}{\sum_{p \in \mathbf{P}} D(p)^2} \quad (40)$$

where  $p$  is a pixel location,  $p'$  is the new center,  $\mathbf{P}$  is the set of pixel locations selected via thresholding,  $D(p)$  is the shortest distance from  $p$  to the closest center

already chosen, and  $D(p')$  is the shortest distance from  $p'$  to the closest center already chosen [31]. Even though k-means++ also relies on the number of targets as an input, overestimating a value for  $k$  will ultimately generate multiple estimated target locations that are approximations of the true target locations.

### III. Methodology

The work performed in this thesis depended on choosing which RTI models to implement in conjunction with which reconstruction methods. Making the decision pertaining to which models to implement was based on model performance and which parameters could be logically compared. Making the decision pertaining to which reconstruction methods to implement was based on multipath mitigation and computational complexity.

Along with selecting the RTI models and reconstruction methods, it was necessary to make other choices pertaining to RTI performance and analysis. Five performance metrics were chosen to quantitatively analyze the performance of each model and reconstruction method combination. The RTI regularization and width of the ellipse parameters were also chosen to enhance the performance of each model and reconstruction method combination. The rest of this chapter discusses the cylindrical human model used to simulate the human targets, the RTI data collection process used to record the RSS measurements, and the k-means++ algorithm used to calculate the estimated target locations.

#### 3.1 RTI Models Chosen

The NeSh and weighting-g models were chosen to generate different weight matrices that impact the model for the change in RSS. The NeSh model was chosen because it is the most common RTI model that successfully employs an ellipse to simplify determining which pixels lie along the LOS path [1]. It also mitigates multipath interference by assigning zero weights to the pixels along the NLOS paths. The weighting-g model was chosen because it too utilizes the ellipse and this common feature allows the models and their results to be logically compared. Also, the

weighting-g model more accurately weights the pixels by assigning values based on the distance between each pixel inside the ellipse and the LOS path [16]. For both models, equations (9) and (15) reveal the pixels that do not lie along the LOS paths are assigned zero weights and the zero weights suppress multipath interference.

### 3.2 RTI Reconstruction Methods Chosen

Tikhonov regularization and LRSD were chosen as the reconstruction methods to generate the attenuation images used for target localization. Tikhonov regularization was chosen based on its regularization parameter, linearity, and reduced computational complexity. The regularization parameter  $\alpha$  is responsible for suppressing the noise spikes and smoothing the attenuation image to clearly display the target boundaries without noise significantly interfering. The linearity leads to faster reconstruction because instantaneous measurements are not necessary to solve for  $\Pi$  in equation (22) [1]. The linearity also contributes to reduced computational complexity because the estimated attenuation image is solved from the simplified transformation in equation (21). The LRSD reconstruction method was chosen based on its multipath mitigation. LRSD suppresses the multipath interference by implementing a low-rank condition on the background image. It then enhances the target-induced attenuation by implementing sparsity-regularized methods on the foreground image [2]. LRSD increases the target localization accuracy by decreasing the prevalence of noise in the attenuation image.

### 3.3 Performance Metrics

The performance metrics were used to generate quantitative results for the purpose of comparing the true attenuation images and true target locations to the estimated attenuation images and estimated target locations. Each performance metric utilized

information from the attenuation images, target locations, or algorithms. In this way, each model and reconstruction method combination was evaluated across a diverse set of performance parameters.

### 3.3.1 Image Mean-Squared Error

The mean-squared error (MSE) performance metric was used to determine the image quality of the estimated attenuation image  $\hat{\mathbf{x}}$ . The MSE formula is given by

$$\tau = \frac{\|\mathbf{x}_c - \hat{\mathbf{x}}_{Norm}\|^2}{N} \quad (41)$$

where  $\mathbf{x}_c$  is the normalized true image with subscript  $c$  referring to the human cylindrical model to be discussed in section 3.5,  $\hat{\mathbf{x}}_{Norm}$  is the normalized estimated image, and  $N$  is the total number of pixels in the image [1, 32]. For the same target scenario, the RTI model and reconstruction method combinations were implemented to generate different estimated attenuation images. The MSEs of these estimated attenuation images were then compared. The optimum MSE value was the lowest of them all and indicated the respective RTI model and reconstruction method combination produced the estimated attenuation image that was most similar to the true attenuation image.

### 3.3.2 Dispersion

According to [33], dispersion measures the spread of the pixels that represent each target in the attenuation image. The pixels that represent each target are known as the target pixels and are filtered via thresholding. The pixel locations with pixel intensities greater than or equal to the threshold retain their normalized value and signify the target pixels. The pixel locations with intensities that fail to meet the

threshold are eliminated. The dispersion  $\sigma_{Centroid}$  is yielded by

$$\sigma_{Centroid} = \sqrt{\frac{\sum_{j=1}^N \|K_j - v\|^2 \cdot \hat{x}_j}{\sum_{j=1}^N \hat{x}_j}} \quad (42)$$

where  $K_j$  is the coordinate of the  $j^{th}$  pixel,  $v$  is the centroid coordinate location,  $\hat{x}_j$  is the intensity of the  $j^{th}$  pixel in the normalized estimated attenuation image after thresholding, and  $N$  is the total number of pixels selected via thresholding [33]. The dispersion of each estimated target in  $\hat{\mathbf{x}}_{Norm}$  was calculated and compared to the dispersion of each true target in  $\mathbf{x}_{Norm}$ . The dispersion error was calculated using

$$\sigma_{error} = |\sigma_{Centroid} - \hat{\sigma}_{Centroid}| \quad (43)$$

where  $\sigma_{Centroid}$  is the dispersion of the true target in  $\mathbf{x}_{Norm}$  and  $\hat{\sigma}_{Centroid}$  is the dispersion of the estimated target in  $\hat{\mathbf{x}}_{Norm}$ .

### 3.3.3 Target Location Root-Mean-Squared Error

The root-mean-squared error (RMSE) was used to measure the error between the true target location(s) and estimated target location(s). The RMSE is given by

$$RMSE = \sqrt{\frac{\sum_{m=1}^M (\|\hat{\mathbf{z}}_m - \mathbf{z}_m\|)^2}{M}} \quad (44)$$

where  $\hat{\mathbf{z}}_m$  is the  $m^{th}$  estimated target location,  $\mathbf{z}_m$  is  $m^{th}$  true target location, and  $M$  is the total number of true and estimated target locations [14]. For the same target scenario, the RTI model and reconstruction method combinations were implemented to generate different estimated attenuation images. The RMSEs of these estimated attenuation images were then compared. The optimum RMSE value was the lowest of them all and indicated the respective RTI model and reconstruction method com-

bination produced the most accurate target localization out of the results compared.

### 3.3.4 Execution Time

Execution time is the measure of how fast programming code runs. For this thesis, the execution time measured the speed of each written MATLAB function. The Tikhonov function was written to average the RSS data across multiple frames, calculate the change in RSS using the averaged RSS data and calibration data, calculate the weight matrices for the Nesh and weighting-g models, and implement Tikhonov regularization using both models. The LRSD function included the same tasks except LRSD was implemented using the NeSh and weighting-g models. The built in MATLAB function *profile* was used to measure the execution time of each function. Execution time is a common performance metric as demonstrated by its use in [32, 34, 35, 36, 37].

## 3.4 RTI Parameters Chosen

A wide range of regularization parameters  $\alpha$  were tested to determine the proper amount of smoothing for the attenuation images. A wide range was chosen because values that were too small made it difficult to distinguish whether a bright pixel was noise or a target. Also,  $\alpha$  values that were too large made the image so smooth that it became difficult to determine the target boundaries [1].

The width of the ellipse  $\lambda$  played a vital role in determining the pixels included on the LOS path. When  $\lambda$  was too large, the pixels on the NLOS path were included even though attenuation may or may not have occurred at those locations. Also, when  $\lambda$  was too small, some of the pixels that in fact made up the LOS path were excluded and resulted in loss of attenuation information [1].

### 3.4.1 Regularization Parameter

Experimental testing was conducted using a range of 10 to 10,000 to choose the regularization parameter  $\alpha$ . Figure 7 illustrates attenuation images with different  $\alpha$  values and smoothing results. For Tikhonov regularization, the final  $\alpha$  values chosen were 1,000 for the NeSh model and 10,000 for the weighting-g model. One reason for the difference was that the weighting-g model attenuation factor  $e^{-h}$  required a larger  $\alpha$  value in order for the attenuation images to have proper smoothing. Figure 8 (d) illustrates an example of an attenuation image with proper smoothing for the weighting-g model and Tikhonov regularization. For LRSD, the  $\alpha$  value was set to 0.25 for both models based on the algorithmic information given in [2].

### 3.4.2 Width of the Ellipse

For the NeSh and weighting-g models, experimentation of the  $\lambda$  values was conducted to determine which values produced sufficient results for single and two-target scenarios. For the NeSh model, the  $\lambda$  values ranged from 0.01 to 0.1 feet with 0.01 feet increments. The decision to use this range was based on [1] conducting experiments with a  $\lambda$  value of 0.01 feet in one scenario and 0.07 feet in another. The variation in  $\lambda$  demonstrated the width of the ellipse was scenario dependent. Also, the range did not consist of  $\lambda$  values smaller than 0.01 feet because values that were too small excluded pixels that made up the LOS path. Figure 9 illustrates the NeSh model weighted links for three different  $\lambda$  values. The smallest value is half the size of 0.01 feet and the largest is twice the size of 0.01 feet. For the weighting-g model, the  $\lambda$  values ranged from 0.05 to 0.14 feet with 0.01 feet increments. This decision was based on [16] conducting experiments with a  $\lambda$  value of 0.05 feet. Figure 10 illustrates the weighting-g model weighted links for three different  $\lambda$  values. The smallest value is half the size of 0.05 feet and the largest is twice the size of 0.05 feet.

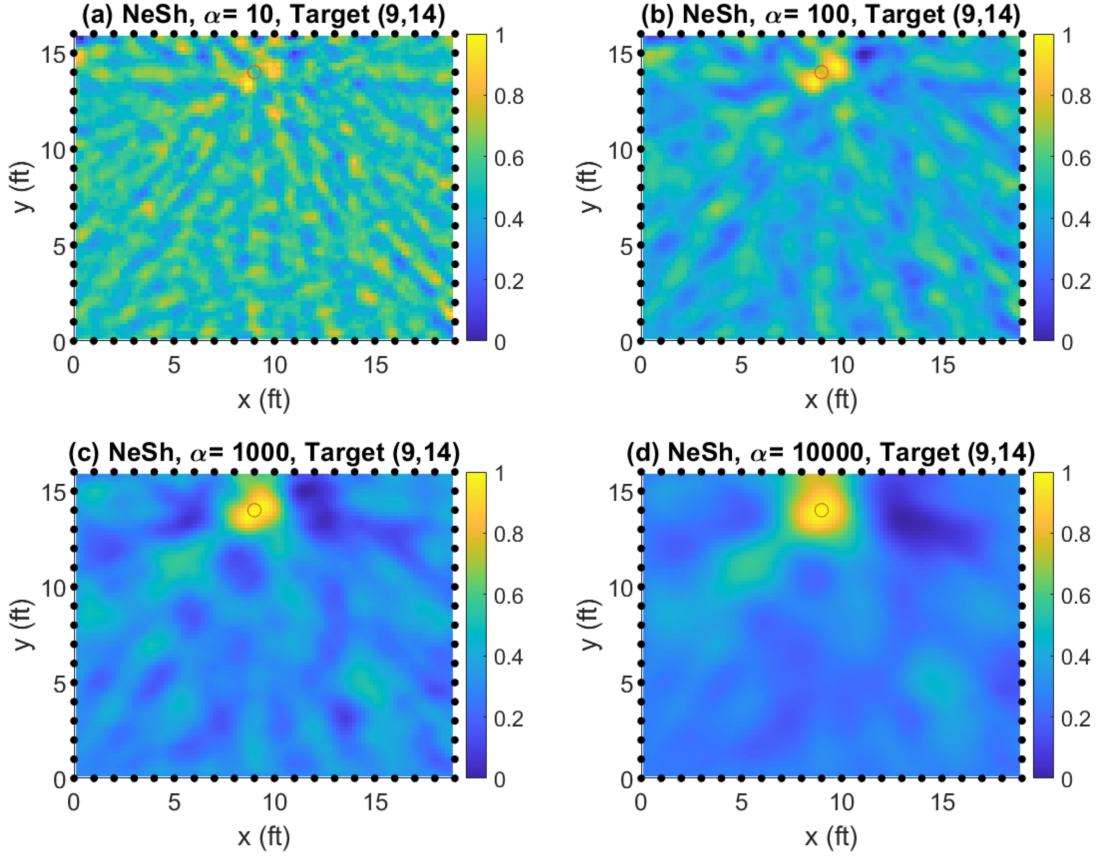


Figure 7: NeSh model and Tikhonov regularization attenuation images for  $\alpha$  values of 10 (a), 100 (b), 1,000 (c), and 10,000 (d).

The widths of the ellipses for the NeSh and weighting-g models were chosen based on the MSE, RMSE, and dispersion error performance metrics. These metrics were chosen based on their results alluding to image and target localization accuracy. The ranges of  $\lambda$  values previously discussed for the RTI models were tested for six different target scenarios. The testing was conducted by implementing the models and their respective parameters in conjunction with Tikhonov regularization and LRS. Three of the six target scenarios were single target scenarios for true target locations (9,14), (5,5), and (15,8). The last three were two-target scenarios for true target location pairs (2,8) (5,10), (2,10) (15,12), and (11,4) (11,14). The respective  $\alpha$  values of 1,000, 10,000, and 0.25 remained constant. After implementing the combinations to test

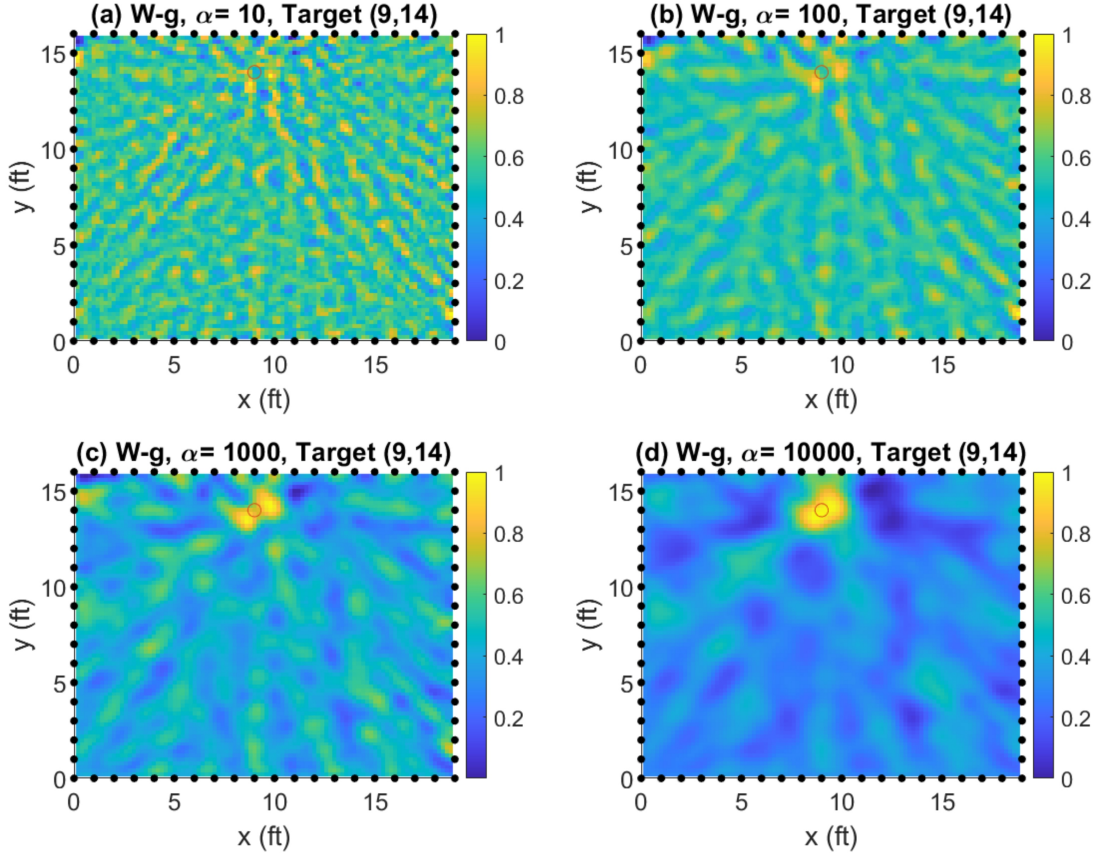


Figure 8: Weighting-g model and Tikhonov regularization attenuation images for  $\alpha$  values of 10 (a), 100 (b), 1,000 (c), and 10,000 (d).

the two ranges of 10  $\lambda$  values, the performance metrics were calculated to yield 60 MSEs, 90 RMSEs, and 90 dispersion errors for each combination. The RMSEs and dispersion errors each totaled 90 because there were 30 results for the three single target scenarios and 60 results for the three two-target scenarios. When each  $\lambda$  value was tested for each two-target scenario, the two individual RMSEs and two individual dispersion errors were averaged together respectively. The end result was a total of 60 MSEs, 60 RMSEs, and 60 dispersion errors for each combination. Next, the average errors were calculated across all six target scenarios resulting in 10 MSEs, 10 RMSEs, and 10 dispersion errors for each combination. The  $\lambda$  values corresponding to lowest MSE, RMSE, and dispersion error were selected. These three selected  $\lambda$  values were

then averaged together and rounded to the nearest hundredth to determine the final  $\lambda$  value for each RTI model and reconstruction method combination. The final  $\lambda$  results for the NeSh model were 0.02 feet for Tikhonov regularization and 0.05 feet for LRSD. The final  $\lambda$  results for the weighting-g model were 0.05 feet for Tikhonov regularization and 0.09 feet for LRSD.

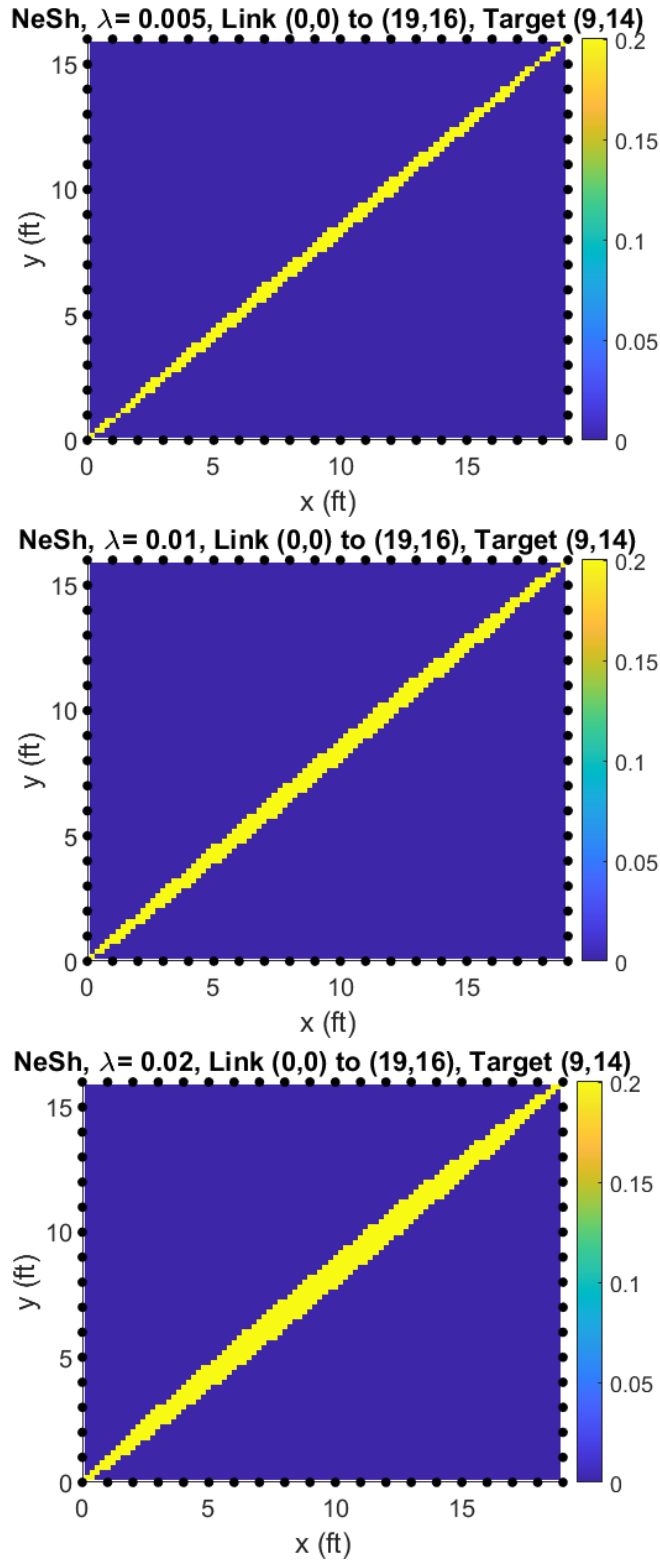


Figure 9: Images of NeSh model weighted links for  $\lambda$  values of 0.005 (top), 0.01 (middle), and 0.02 (bottom) for an example link.

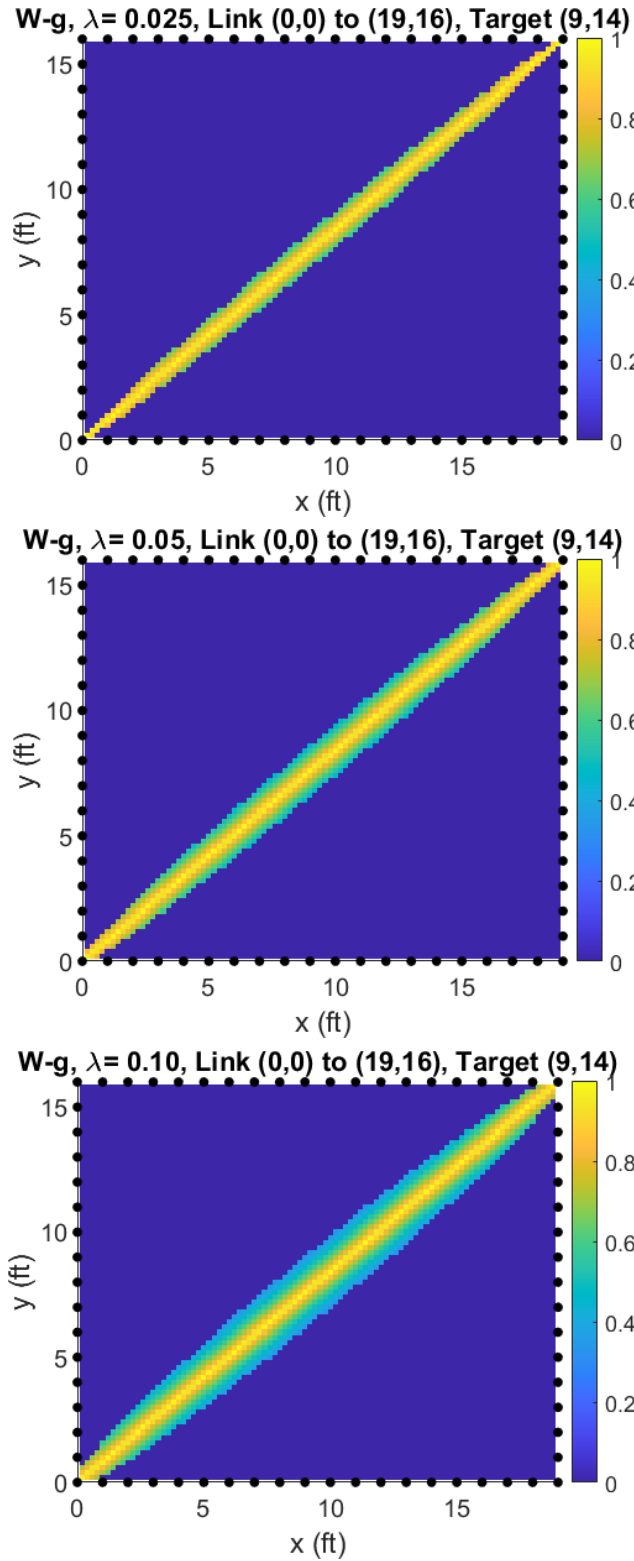


Figure 10: Images of weighting-g model weighted links for  $\lambda$  values of 0.025 (top), 0.05 (middle), and 0.10 (bottom) for an example link.

### 3.5 Cylindrical Human Model

For the purpose of this thesis, the target is a human represented by an attenuating cylindrical model. This model was selected because it is a simple way to represent the size, shape, and attenuation of the human body [1]. The normalized true attenuation image  $\mathbf{x}_c$  of a human target in the RTI WSN is represented by

$$\mathbf{x}_{cj} = \begin{cases} 1, & \text{if } \|\mathbf{x}_j - \mathbf{c}_H\| < R_H \\ 0, & \text{otherwise} \end{cases} \quad (45)$$

where  $\mathbf{x}_{cj}$  is the center of pixel  $j$ ,  $\mathbf{x}_j$  is the location of pixel  $j$ ,  $\mathbf{c}_H$  is the true target or human location, and  $R_H$  is the human radius [1, 2]. The human radius is 1.3 feet in accordance with [1]. Figure 11 is an example of the true attenuation image produced after implementing equation (45). The true image  $\mathbf{x}_c$  and true target location(s) are necessary to compute the MSE, RMSE, and dispersion.

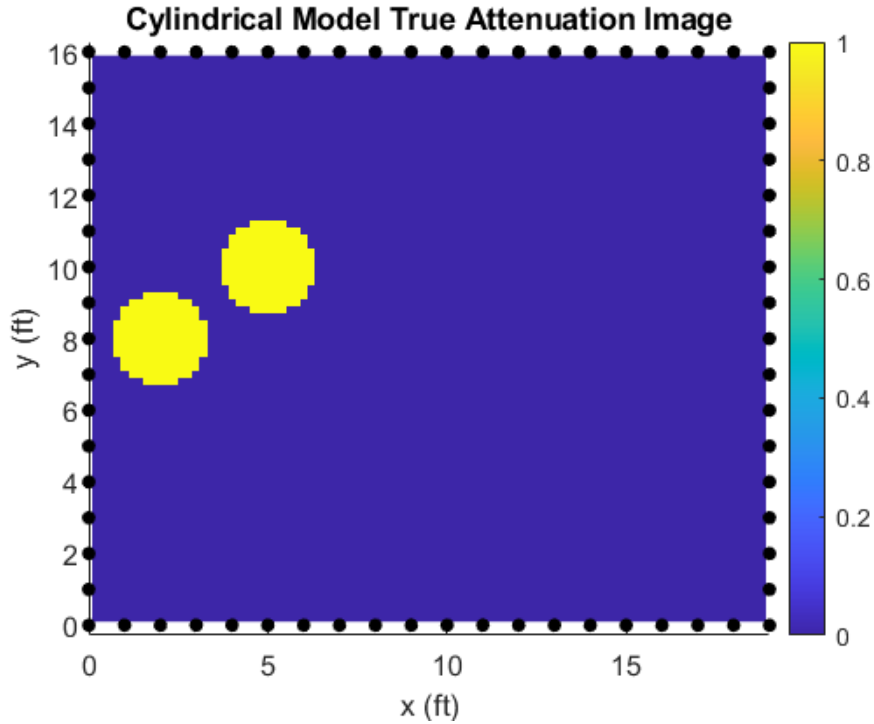


Figure 11: True attenuation image for target locations (2,8) and (5,10).

### 3.6 RTI Data Collection

The RSS data used in this thesis was collected by Jeffrey Nishida and Tan Van at the Air Force Institute of Technology (AFIT). The RTI system in the AFIT laboratory consisted of 70 TelosB TPR2400CA transceivers manufactured by MEMSIC. The transceivers communicated using the Spin protocol and operated on the 2.4 GHz band [38]. They were mounted at 3'4" on polyvinyl chloride (PVC) pipes.

The experimental data was collected by using the RTI system for single and multi-target scenarios. The laboratory environment surrounding the RTI system consisted of metal file cabinets and racks that introduced more multipath interference. For most of the data sets, multipath interference may have contributed to 5% – 10% of unreported RSS data for some of the links. The links with unreported RSS data were assigned NaN arguments. There were 27 iterations or frames of data collected for each

scenario. There was also one frame of calibration data collected before any targets were positioned in the scenes. To improve the experimental data used in this thesis, the unreported RSS data denoted by NaN was replaced with the corresponding RSS data recorded in the previous frame. For each target scenario, the 27 frames of RSS data were averaged together to form the improved data sets used for processing.

### 3.7 K-Means++

The k-means++ algorithm was chosen for target localization. This algorithm was chosen over HAC because of its fast execution time and simple application in MATLAB using the *kmeans* function. Although k-means++ still requires an input for  $k$ , if the value for  $k$  is overestimated the algorithm will generate multiple estimated target locations that are approximations of the true target location(s). Figure 12 illustrates examples of using k-means++ to produce 10 target location estimates although there are only one (left) and two (right) targets located in the attenuation images. These estimated target locations surround the true target locations and form groups. The true target locations can be further approximated by computing the averages of the groups of estimated target locations. Also, thresholding was performed to only include the pixels with normalized intensities of 0.7 or greater as potential cluster centers. The normalized pixel intensity of 0.7 was chosen because higher thresholds eliminated pixels with target-induced attenuation.

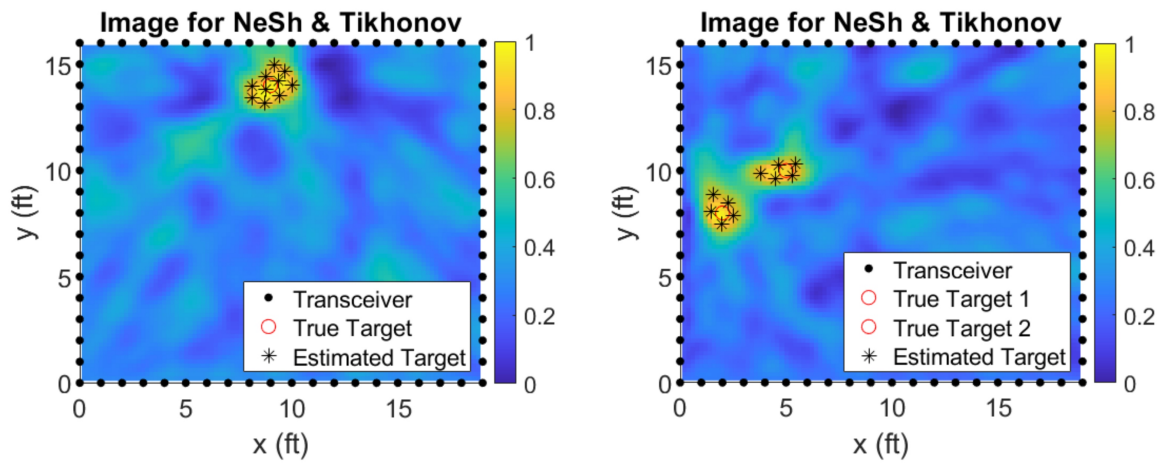


Figure 12: Attenuation image for true target location (9,14) with  $k = 10$  estimated target locations (left) and attenuation image for true target locations (2,8) and (5,10) with  $k = 10$  estimated target locations (right).

## IV. Results and Analysis

### 4.1 Attenuation Image Results

The attenuation images were analyzed qualitatively using visual inspection and quantitatively using the metrics discussed in Chapter III. The qualitative analysis was conducted based on the author’s background knowledge of optimum RTI attenuation images discussed in literature such as [1], [2], and [16]. Optimum RTI attenuation images have low noise prevalence, clear target boundaries, and estimated target locations represented by the highest intensity target pixels.

Each figure in this chapter includes a group of four attenuation images for one of the six target scenarios. For each figure, the Tikhonov regularization images are in the left column and the LRSD images are in the right column. The NeSh model images are in the first row and the weighting-g model images are in the second row. Throughout the rest of this thesis, the RTI model and reconstruction method combinations will be referred to by the following acronyms:

- N-T: NeSh model in conjunction with Tikhonov regularization
- W-T: Weighting-g model in conjunction with Tikhonov regularization
- N-L: NeSh model in conjunction with LRSD
- W-L: Weighting-g model in conjunction with LRSD.

#### 4.1.1 Target Location (9,14)

Figure 13 illustrates the attenuation images generated for the true target located at (9,14). In the figure, the W-L image has more dark blue pixels than the other images. These dark blue pixels have intensities of 0 to 0.1 and are indicative of no

attenuation which should be expected for pixels that lie along links the target does not interfere with. This is also consistent with the true attenuation image which has dark blue pixels with intensities of zero to represent the absence of target-induced attenuation (figure 11). The greater number of dark blue pixels suggests lower noise prevalence in the W-L image.

Figure 14 is a magnified version of the attenuation images in figure 13. The x and y axes have been reduced to only include the pixels that are closest to the true target location. In the figure, the N-T, W-T, and W-L images have clear target boundaries formed by the target clusters with individual pixel intensities of 0.07 or greater. Also, the N-T and W-T images have significantly more bright yellow target pixels with

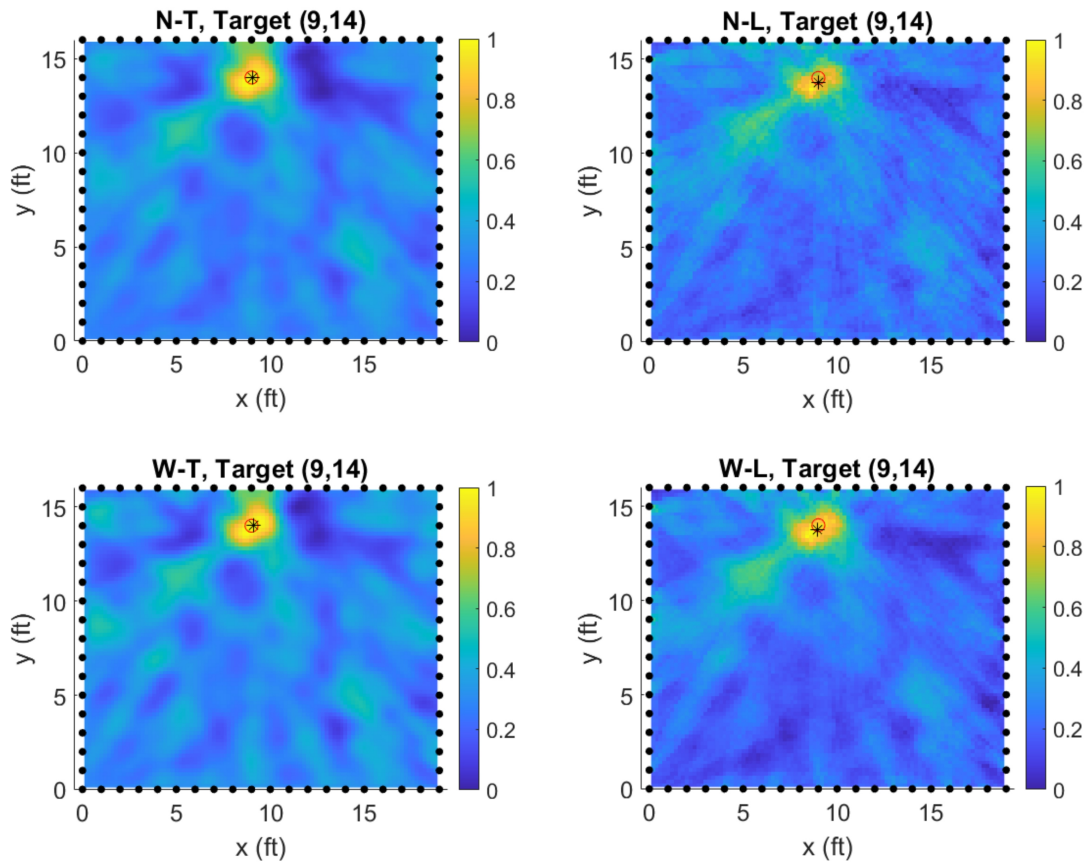


Figure 13: Attenuation images for target location (9,14).

intensities of 0.9 to 1 centered around the true target location. These high intensity pixels are indicative of target-induced attenuation which is consistent with the true image. The N-T image has the most accurate estimated target location represented by the black asterisk inside of the red circle which represents the true target location (9,14). Visually, the W-L image has the lowest noise prevalence while the N-T image has significantly more bright yellow target pixels and the highest target localization accuracy.

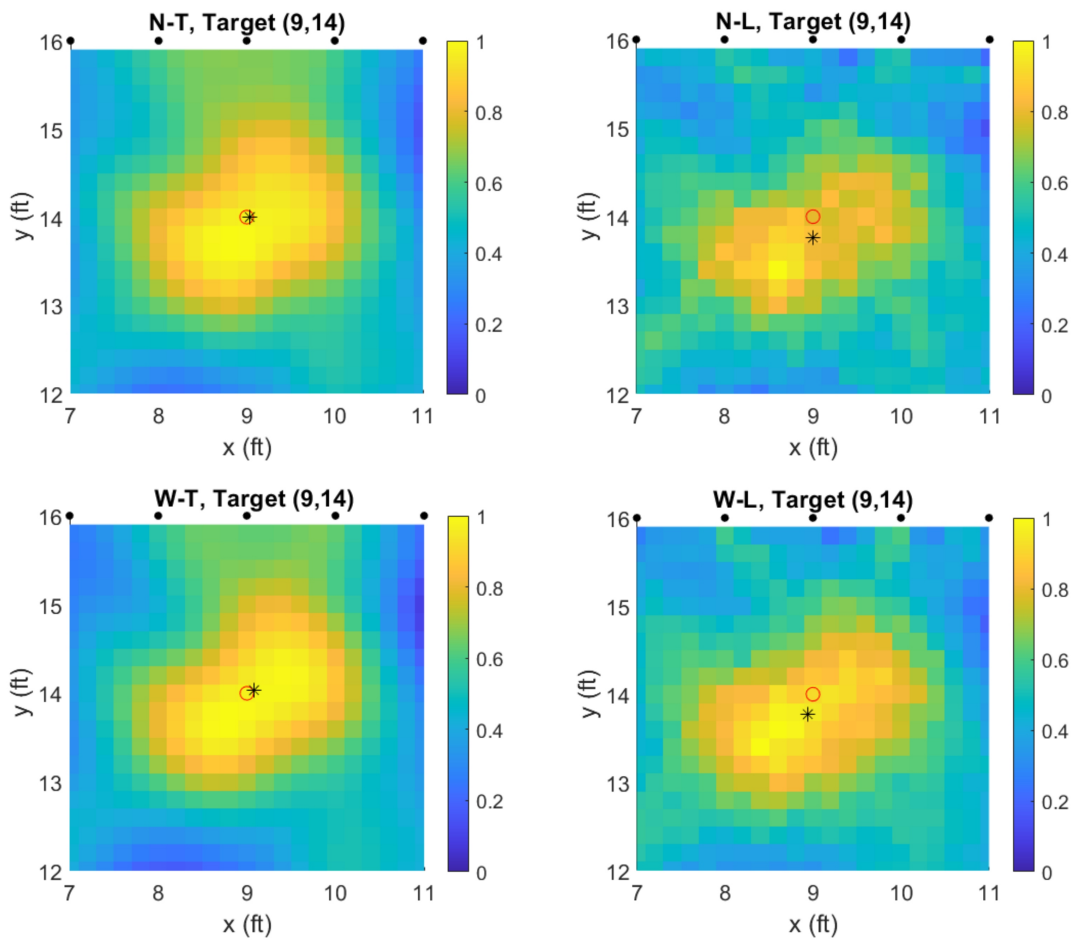


Figure 14: Magnified attenuation images for target location (9,14).

### 4.1.2 Target Location (5,5)

In figure 15, the N-T and W-T images appear to have the most dark blue pixels. However, they also have green and yellow pixels with intensities of 0.6 to 1 in areas that are not close to the true target at (5,5). These areas of excess attenuation are imaging artifacts that can degrade image and target localization accuracy. Therefore, the N-L and W-L images have the lowest noise prevalence because they do not contain those imaging artifacts.

Figure 16 provides an enhanced illustration of the target boundaries and higher intensity pixels. The N-T and W-T images have more distinct target boundaries

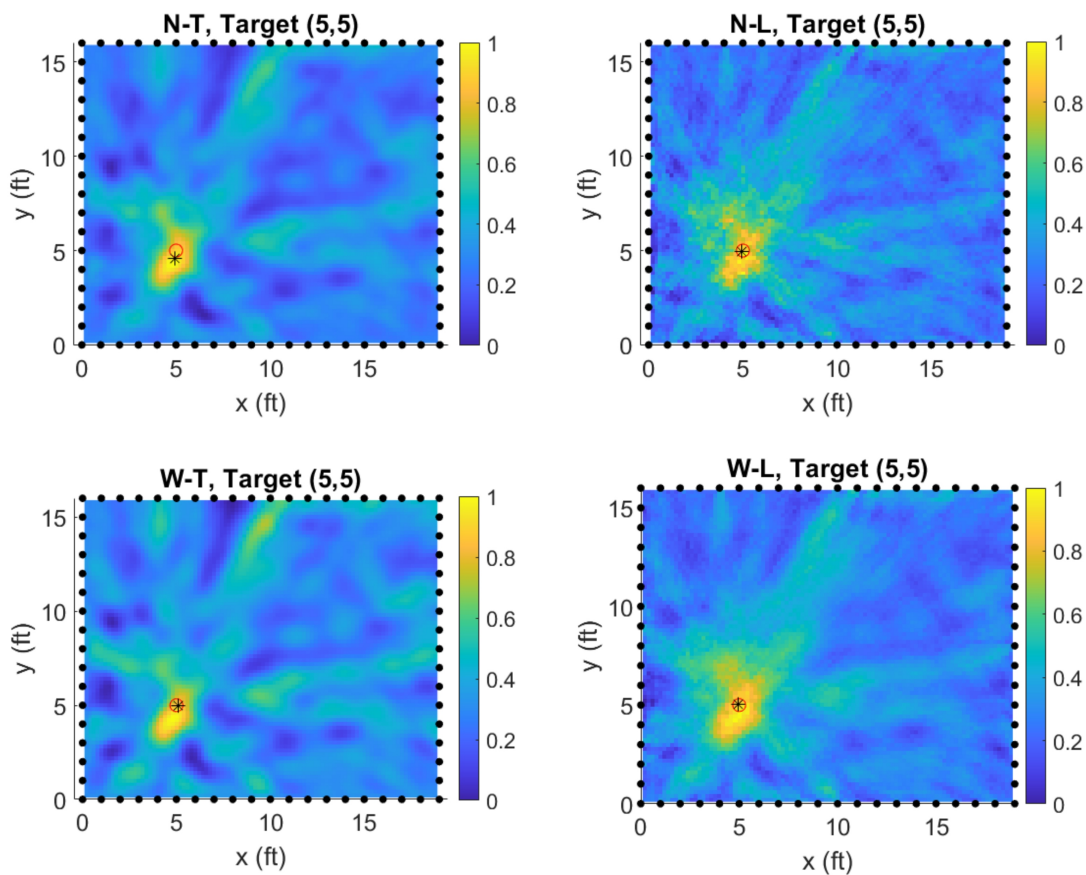


Figure 15: Attenuation images for target location (5,5).

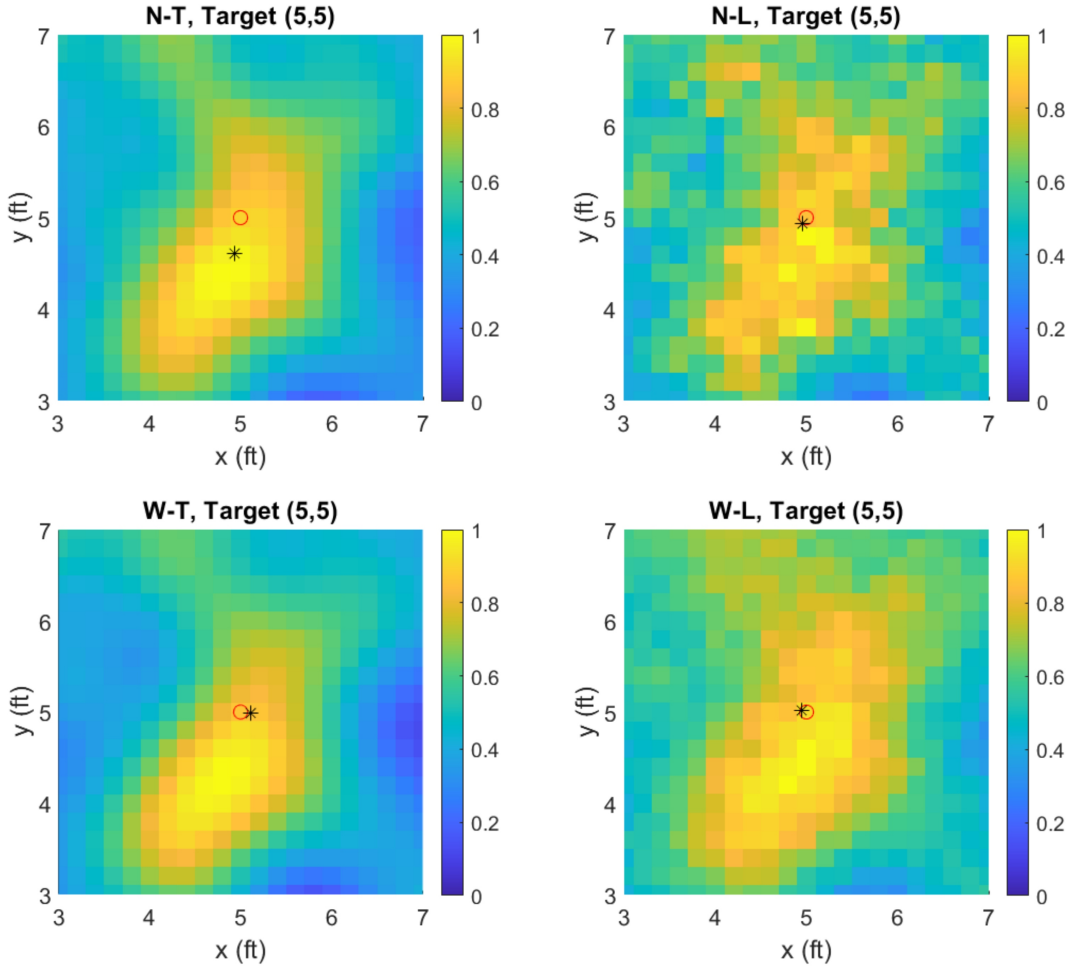


Figure 16: Magnified attenuation images for target location  $(5,5)$ .

compared to the sparse target cluster in the N-L image and the far spread target cluster in the W-L image. The N-T and W-T images also have more bright yellow target pixels with intensities of 0.9 to 1 than the other two images. However, the bright yellow target pixels in the N-T and W-T images are clustered below the true target location, whereas in the W-L image the bright yellow target pixels are located closer to  $(5,5)$ . The estimated target locations represented by the black asterisks in the N-L and W-L images are the closest approximations to the true target location  $(5,5)$ . Visual inspection suggests the N-L and W-L images have the lowest noise prevalence and highest target localization accuracy.

### 4.1.3 Target Location (15,8)

The N-L and W-L images have the lowest noise prevalence in figure 17. This is evident by the greater number of dark blue pixels in the N-L and W-L images than in the N-T and W-T images. The N-T and W-T images also have more green pixels that represent imaging artifacts near the true target location.

In figure 18, the target boundaries are more clearly defined for the N-T, W-T, and W-L images. The N-T and W-T images also have more bright yellow target pixels compared to the N-L and W-L images. The W-L image has significantly more bright yellow target pixels in the target cluster compared to the N-L target cluster. Using

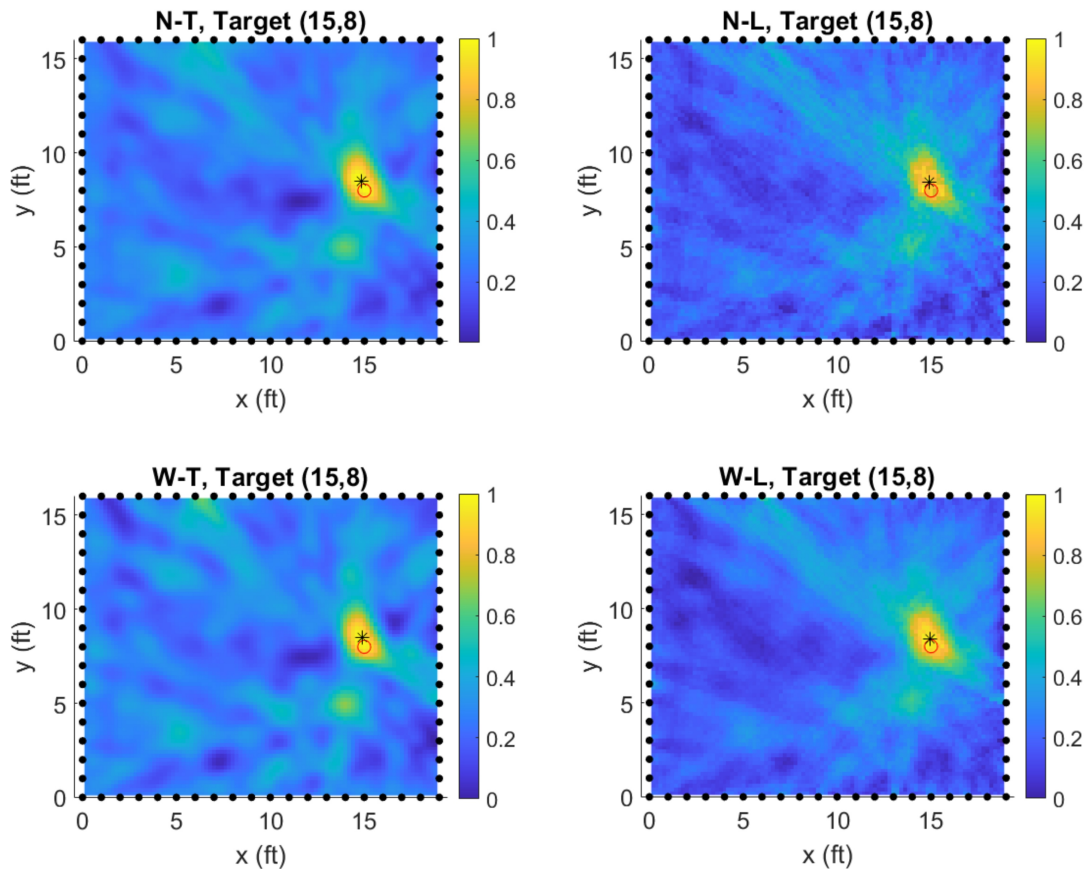


Figure 17: Attenuation images for target location (15,8).

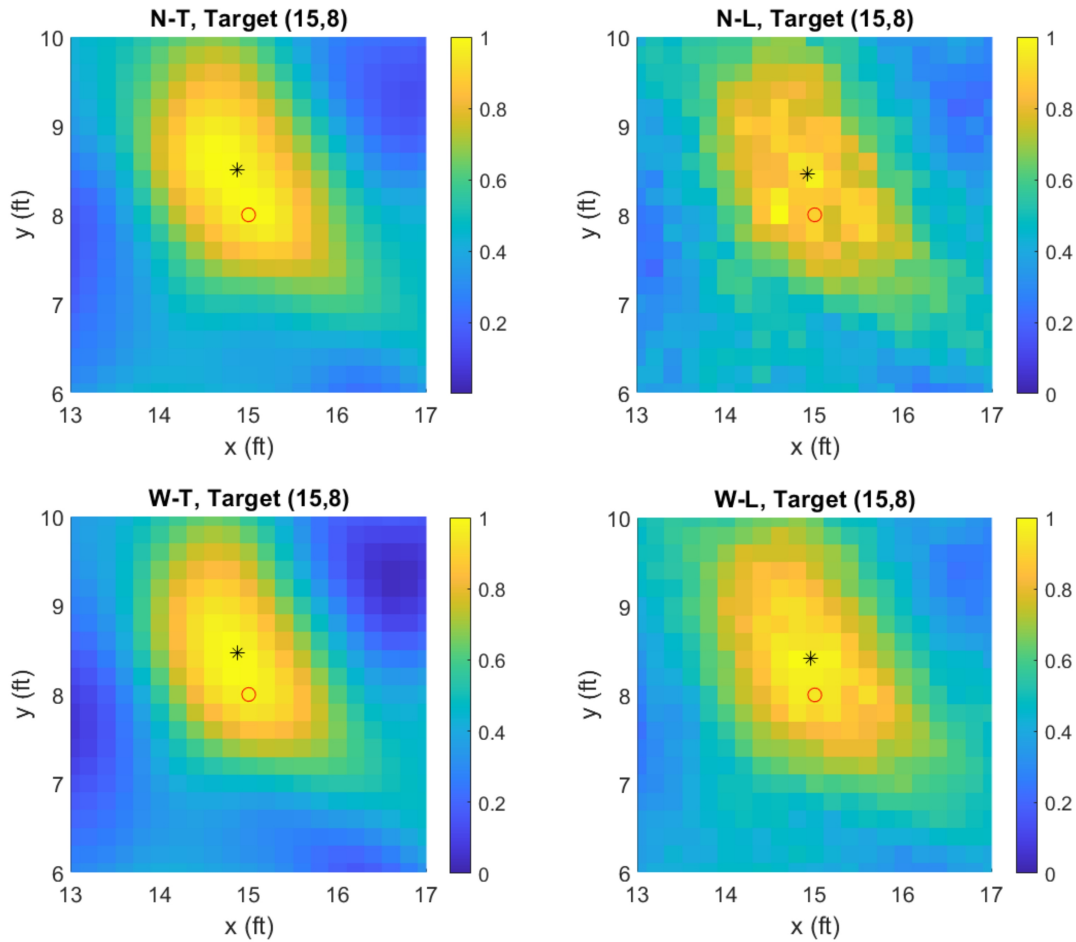


Figure 18: Magnified attenuation images for target location (15,8).

visual inspection, it is very difficult to determine target localization accuracy because all of the estimated target locations are approximately the same distance away from the true target location.

#### 4.1.4 Target Locations (2,8) and (5,10)

In figure 19, the N-T and W-T images have the lowest noise prevalence while the N-L and W-L images have smoother image results. The N-T and W-T images have more dark blue pixels which properly indicate no target-induced attenuation. The N-L and W-L images have more blue pixels with similar intensities of 0.2 to 0.4

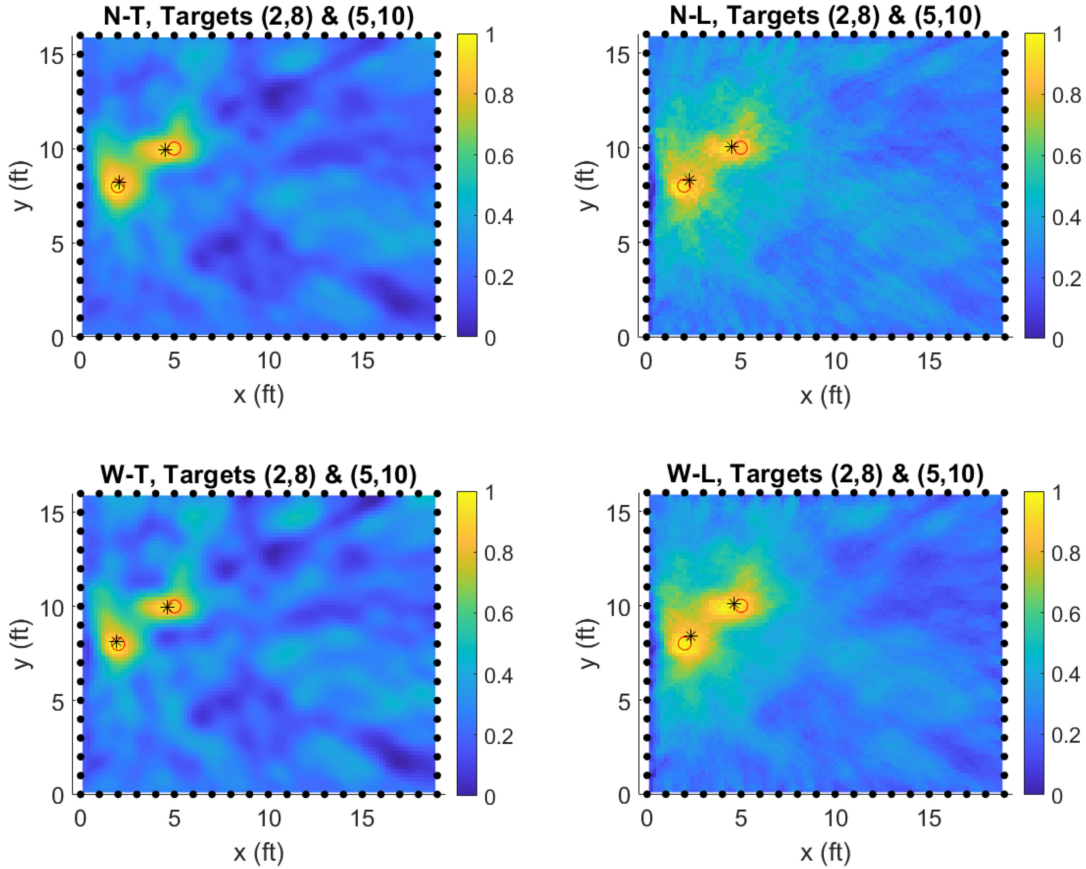


Figure 19: Attenuation images for target locations (2,8) and (5,10).

which create smoother images. Overall, the N-T and W-T images have the lowest noise prevalence because they have more pixels with intensities close to zero.

Figure 20 illustrates the magnified attenuation images in figure 19. The W-T image has the clearest target boundaries. In the N-T, N-L and W-L images, the two target clusters intersect and make the individual target boundaries less distinct. The N-T and W-T images appear to have bright yellow target pixels that are more centrally located around the true target locations. The N-T and W-T images also have more accurate target localization which is evident by the close proximity of the estimated target locations to the true target locations (2,8) and (5,10). Visual inspection suggests the N-T and W-T images have the lowest noise prevalence and

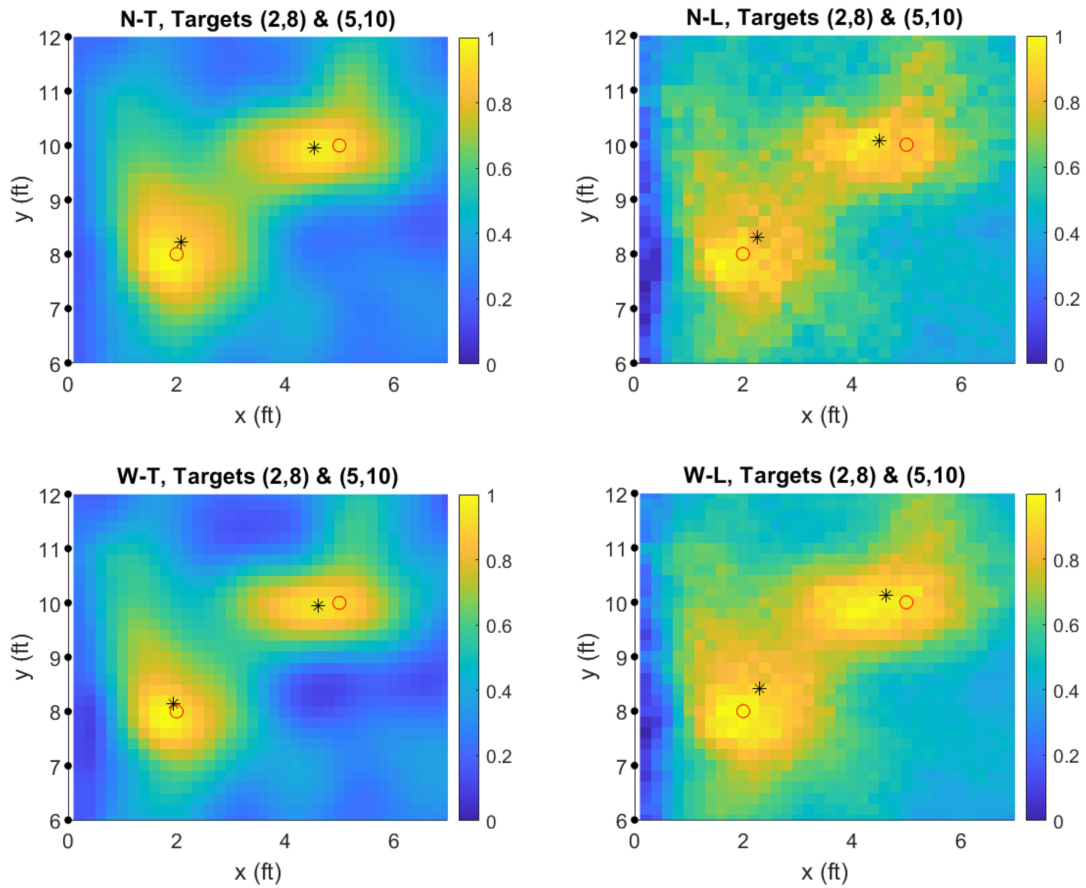


Figure 20: Magnified attenuation images for target locations (2,8) and (5,10).

highest target localization accuracy.

#### 4.1.5 Target Locations (2,10) and (15,12)

In figure 21, the N-T and W-T images have the lowest noise prevalence. They have more dark blue pixels compared to the N-L and W-L images. The N-L and W-L images also have green and dark yellow pixels that represent imaging artifacts around the bright yellow target pixels. Although the N-L and W-L images have fewer dark blue pixels and the presence of imaging artifacts, they also have smoother images due to less variation in the blue pixel intensities.

There is no estimated target location for the true target located at (15,12). The

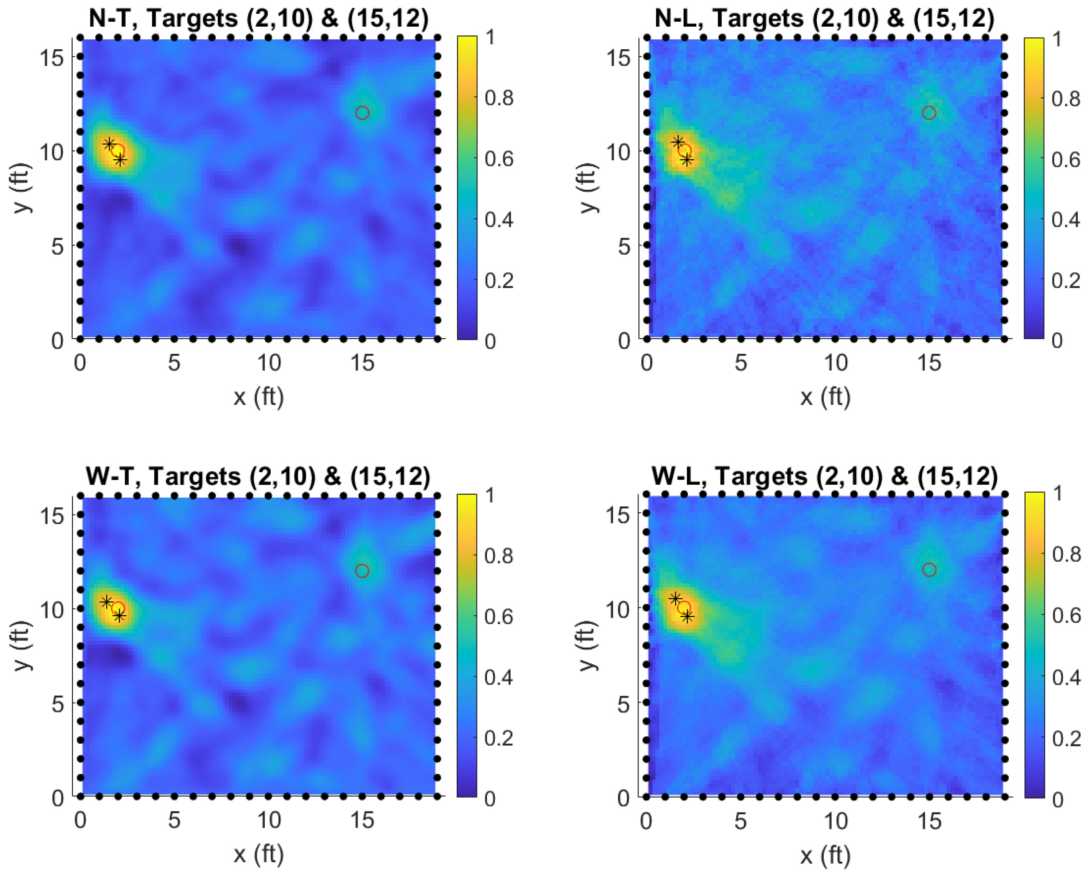


Figure 21: Attenuation images for target locations (2,10) and (15,12).

sensors failed to report the RSS measurements along the links that pass through location (15,12) and those links were assigned NaN arguments. Sensor reporting failure is one of the drawbacks of the RTI system [14]. In this case, the reporting failure resulted in a lack of RSS information which led to the absence of attenuation at location (15,12).

Figure 22 magnifies target location (2,10) in the attenuation images. All four of the images have clear target boundaries. The N-T and W-T images have more bright yellow target pixels closely centered around the true target location. For all four images, it is very difficult to visually determine which image has the highest target localization accuracy. The target localization accuracy is difficult to visually

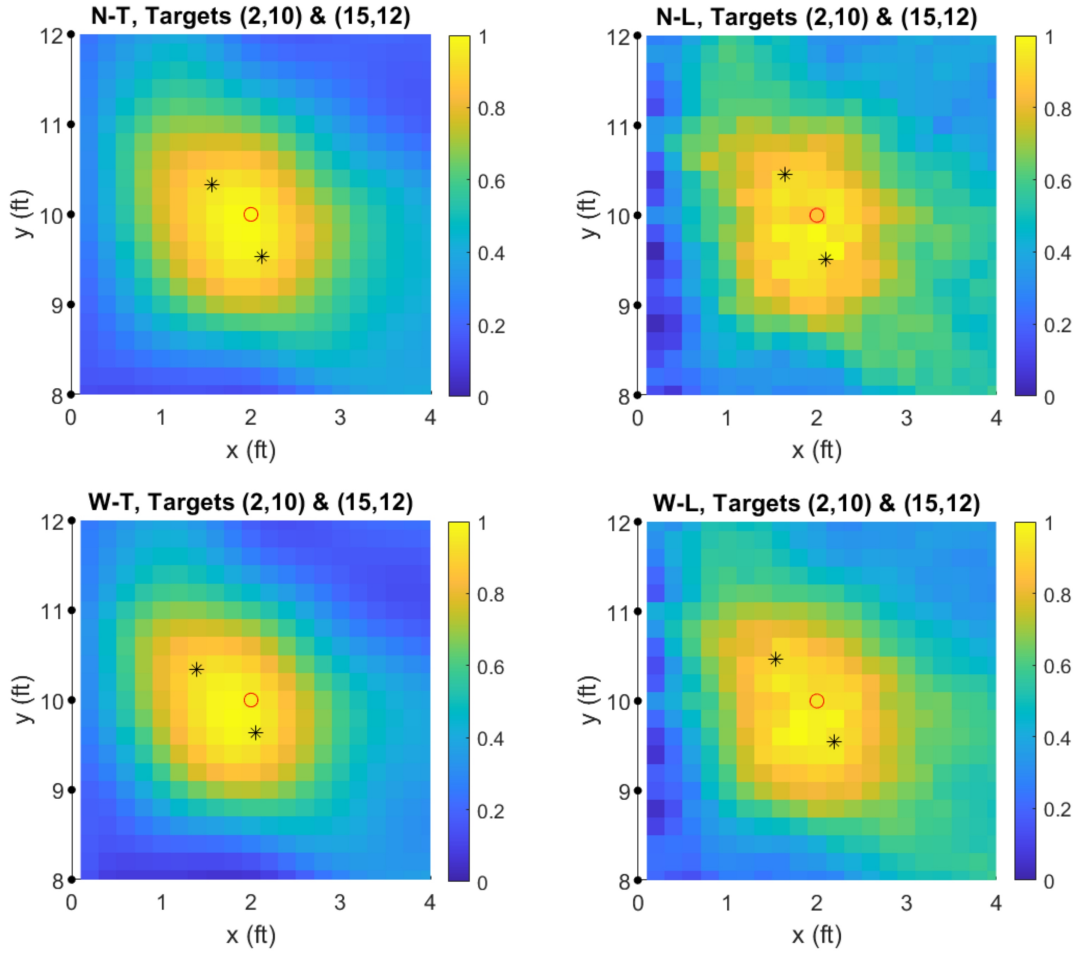


Figure 22: Magnified attenuation images for target location (2,10).

determine because there are two estimated target locations for the target at (2,10) in each image. After thresholding, the k-means++ algorithm determined there were two cluster centers around target location (2,10) because there were no pixels with intensities of 0.7 or greater to represent the attenuation for the target at (15,12). The numerical results in section 4.2 exclude this two-target data set because it introduces significantly higher image and target localization errors as a result of the failed sensor reporting.

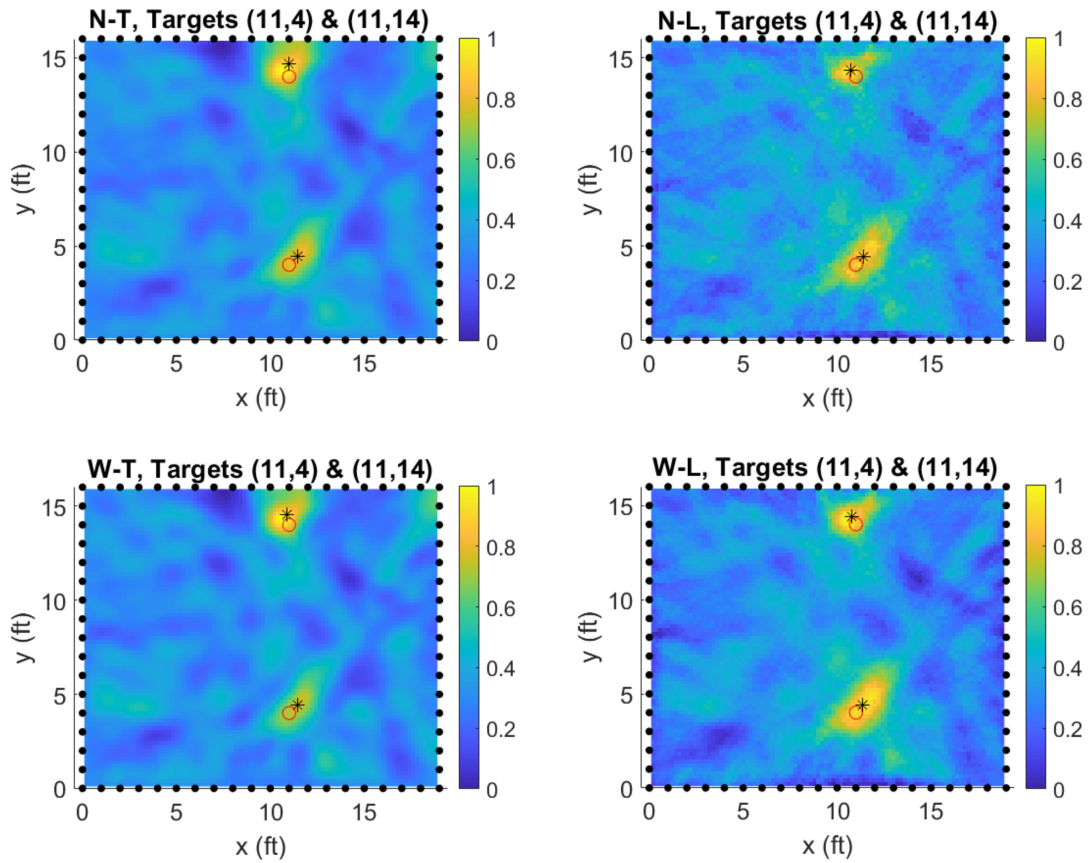


Figure 23: Attenuation images for target locations (11,4) and (11,14).

#### 4.1.6 Target Locations (11,4) and (11,14)

Figure 23 is used to visually analyze the noise prevalence in the attenuation images for target locations (11,4) and (11,14). The W-T and W-L images have the lowest noise prevalence. This is evident by the presence of more dark blue pixels than seen in the other two attenuation images.

Figure 24 is used to visually analyze the target boundaries and the target localization accuracy. The W-L image has the most distinct target boundaries formed by the distinct target clusters. In the N-T and W-T images, the estimated target at (11,4) is represented by lower intensity green and dark yellow pixels that could potentially be mistaken for imaging artifacts. Conversely, the N-L and W-L images

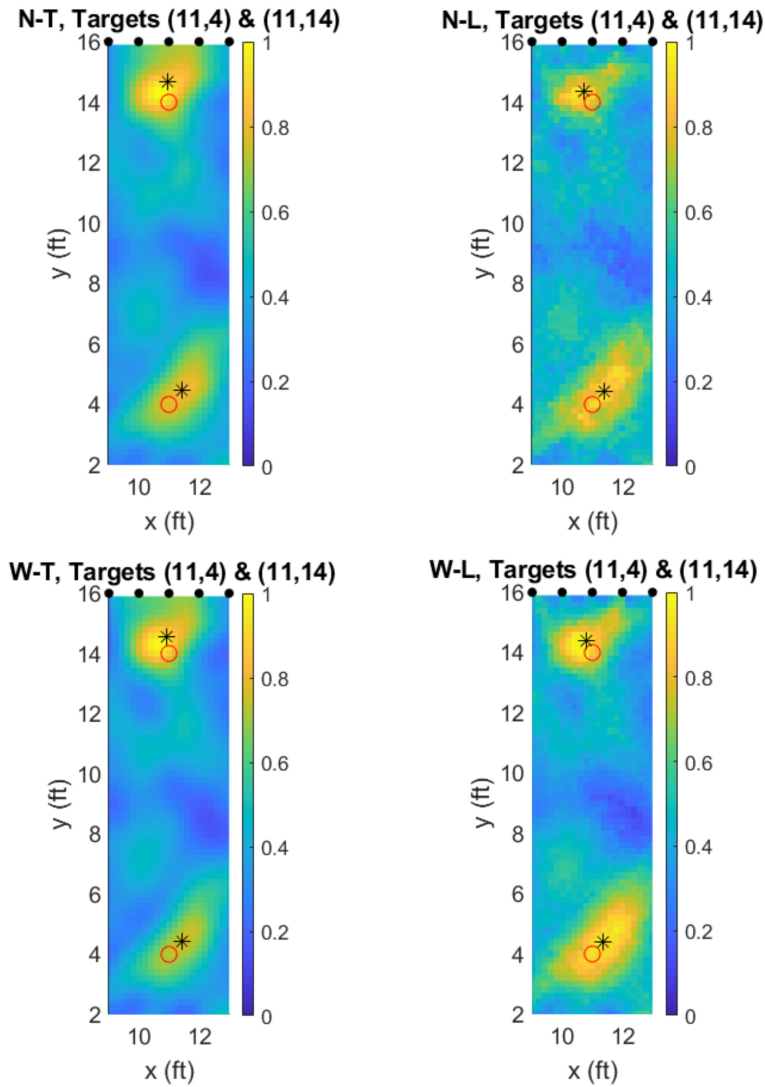


Figure 24: Magnified attenuation images for target locations (11,4) and (11,14).

have higher intensity yellow target pixels surrounding the true target locations. They also have the highest target localization accuracy seen by the close proximity of the estimated target locations to the true target locations (11,4) and (11,14). Overall, visual inspection suggests the W-T and W-L images have the lowest noise prevalence while the N-L and W-L images have the highest target localization accuracy.

## 4.2 Performance Metric Results

The performance metric tables in this chapter display the quantitative results used to determine which RTI model and reconstruction method combinations achieved optimum image accuracy, target localization accuracy, and execution time. The quantitative results were generated using the mathematical formulas discussed in Chapter III. The results can be recomputed and verified by other researchers using the same formulas and data sets. Conversely, the qualitative visual inspection results of the attenuation images are likely to vary amongst researchers based on differences such as training and experience with using the RTI system and analyzing the attenuation image results.

Tables 1 through 5 display the rounded performance metric results for each combination. The numerical values in the rows correspond to each target scenario and the values were rounded to the nearest hundredth to maintain a condensed table size. The performance metric results of the two-target scenario (2,10) and (15,12) were excluded because they introduced significantly higher errors that skewed the average results of the performance metrics. The high errors were a result of the absence of attenuation for target location (15,12) as previously explained in section 4.1.5. The remaining single and two-target scenario performance metric results were averaged together to determine the overall performance of each combination. To compute the averages and standard deviations in the tables, the exact results of the individual target scenarios were used instead of the rounded results displayed in the tables.

### 4.2.1 Image MSE Results

Table 1 provides the MSE results that were used to determine attenuation image accuracy. To calculate the results, the estimated attenuation images were compared to the true attenuation images for five target scenarios. According to the average MSE

Table 1: Image MSE Results

Target(s)	N-T	W-T	N-L	W-L
(9,14)	0.08	0.09	0.07	0.06
(5,5)	0.08	0.10	0.09	0.10
(15,8)	0.08	0.08	0.06	0.06
(2,8) (5,10)	0.06	0.06	0.10	0.09
(11,4) (11,14)	0.09	0.09	0.11	0.09
Average	0.08	0.08	0.09	0.08
Std Dev	0.01	0.01	0.02	0.02

results, the N-T, W-T, and W-L combinations produced the most accurate attenuation images with the lowest average MSE of 0.08. These combinations outperformed the N-L combination by a close margin of 0.01 which is the difference between the rounded averages.

#### 4.2.2 Dispersion Results

Table 2 displays the dispersion results which report how far spread out the target pixels in the attenuation images are. The two individual dispersion results for each two-target scenario were averaged together to generate one average dispersion result for each two-target scenario. Averaging the two individual dispersion results for each two-target scenario was necessary to obtain one result for each of the five target scenarios. Next, the three dispersion results of the single target scenarios and the

Table 2: Dispersion Results (ft). True dispersion is 0.93 ft for all true targets.

Target(s)	N-T	W-T	N-L	W-L
(9,14)	0.83	0.82	0.76	0.81
(5,5)	0.87	2.52	1.08	1.18
(15,8)	0.81	0.77	0.81	0.86
(2,8)	0.81	0.70	1.00	1.07
(5,10)	0.79	0.71	0.99	1.01
(11,4)	0.68	0.53	0.93	1.01
(11,14)	0.80	0.71	0.63	0.70
Average	0.81	1.09	0.88	0.95
Std Dev	0.05	0.81	0.14	0.16

two average dispersion results of the two-target scenarios were used to calculate the average dispersion across all five target scenarios. The W-L combination had an average dispersion of 0.95 feet which was the closest to the true dispersion of 0.93 feet. The dispersion results were not used alone for further image analysis because merely finding the difference between the average dispersion results and the true dispersion was not as meaningful as calculating the individual dispersion error for each target scenario and then averaging those errors together. Therefore, the dispersion error of each target scenario was calculated and also used for comparative analysis.

#### 4.2.2.1 Dispersion Error Results

Table 3 displays the dispersion error results that were used to further analyze image accuracy. The dispersion error was calculated by using equation (43) to find the difference between the dispersion of each estimated target and the dispersion of each true target. All of the true targets had a dispersion of approximately 0.93 feet because the same cylindrical model was used to represent each target at different locations. The two individual dispersion errors for each two-target scenario were averaged together out of necessity as discussed previously in section 4.2.2. For each model and reconstruction method combination, the average dispersion error was computed by

Table 3: Dispersion Error Results (ft)

Target(s)	N-T	W-T	N-L	W-L
(9,14)	0.10	0.11	0.17	0.13
(5,5)	0.06	1.59	0.15	0.25
(15,8)	0.12	0.17	0.13	0.07
(2,8)	0.12	0.24	0.06	0.14
(5,10)	0.14	0.22	0.06	0.08
(11,4)	0.25	0.41	0.01	0.08
(11,14)	0.13	0.22	0.30	0.23
Average	0.12	0.48	0.13	0.14
Std Dev	0.05	0.62	0.04	0.07

averaging the individual error calculations across all five target scenarios. According to table 3, the N-T combination had the lowest average dispersion error of 0.12 feet while the N-L combination was a close second by a margin of 0.01 feet. Accurate dispersion alludes to increased image accuracy because the dispersion calculation (equation 42) relies on the intensities of the pixels that form the target clusters in the attenuation images.

### 4.2.3 Target Location RMSE Results

The target localization accuracy was determined by the RMSE results in table 4. The estimated target locations were compared to the true target locations for the five target scenarios. The two individual RMSE results for each two-target scenario were averaged together out of necessity as previously discussed. The three RMSEs of the single target scenarios and the two average RMSEs of the two-target scenarios were then used to calculate the average RMSE across all five target scenarios. According to table 4, the W-T combination had the most accurate target localization with the lowest average RMSE of 0.22 feet. The W-L combination was a close second by a margin of 0.01 feet.

Table 4: Target Location RMSE Results (ft)

Target(s)	N-T	W-T	N-L	W-L
(9,14)	0.02	0.07	0.17	0.16
(5,5)	0.28	0.08	0.05	0.04
(15,8)	0.37	0.34	0.33	0.29
(2,8)	0.17	0.11	0.29	0.36
(5,10)	0.33	0.28	0.36	0.28
(11,4)	0.45	0.44	0.41	0.39
(11,14)	0.48	0.39	0.31	0.31
Average	0.28	0.22	0.25	0.23
Std Dev	0.16	0.16	0.13	0.13

#### 4.2.4 Execution Time Results

For the five target scenarios, the execution times of the N-T, W-T, N-L, and W-L algorithms are displayed in table 5. According to the table, the algorithms that implemented the weighting-g model ran approximately 50-60 seconds slower than the algorithms that implemented the NeSh model. Overall, the N-L combination had the fastest average execution time of approximately 94 seconds. Although execution time is a key performance metric, a particular scenario could call for increased image and target localization accuracy at the expense of slower execution time. Also, the execution time results depend on the programming platform used and the computation optimization skill of the programmer.

Table 5: Execution Time Results (seconds)

Target(s)	N-T	W-T	N-L	W-L
(9,14)	100.88	157.61	91.63	148.44
(5,5)	93.19	149.72	84.74	139.83
(15,8)	94.56	148.30	84.61	140.32
(2,8) (5,10)	112.12	168.36	103.21	158.19
(11,4) (11,14)	112.44	165.07	103.49	156.90
Average	102.64	157.81	93.54	148.74
Std Dev	9.27	8.95	9.40	8.75

### 4.3 Performance Metric Average Results

Figures 25 through 28 are bar graphs of the performance metric average results for each RTI model and reconstruction method combination. According to figure 25, the N-T, W-T, and W-L combinations all had the lowest average image MSE of 0.08 which indicated high image accuracy. Figure 26 shows the W-L combination had the most accurate average dispersion of 0.95 feet while the N-T combination had the lowest average dispersion error of 0.12 feet. These values allude to increased image accuracy. The figure also shows the W-T combination had the least accurate average dispersion of 1.09 feet and the highest average dispersion error of 0.48 feet. Figure 27 shows the W-T combination had the lowest average target location RMSE of 0.22 feet which indicated high target localization accuracy. According to figure 28, the N-L combination had the fastest average execution time of approximately 94 seconds. Also, the error bars in each figure indicate the standard deviations of the data used to calculate the respective averages.

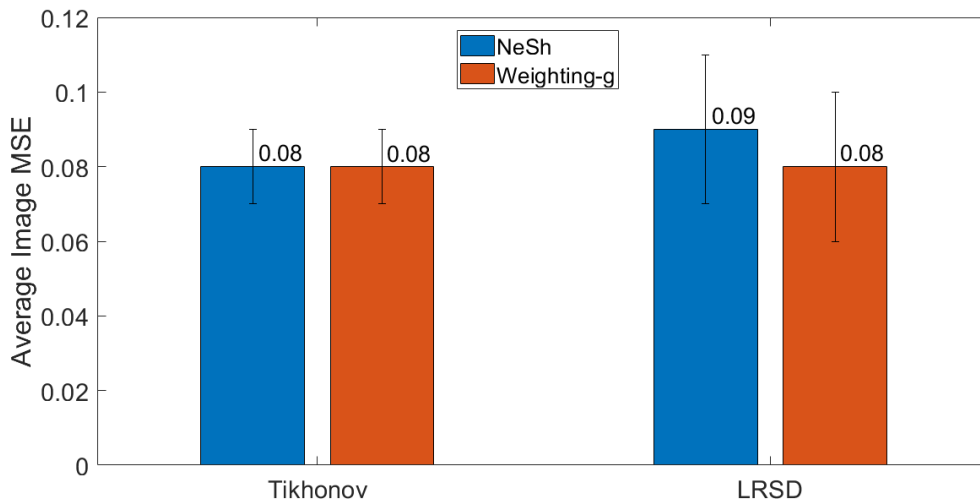


Figure 25: Graph of average image MSE results.

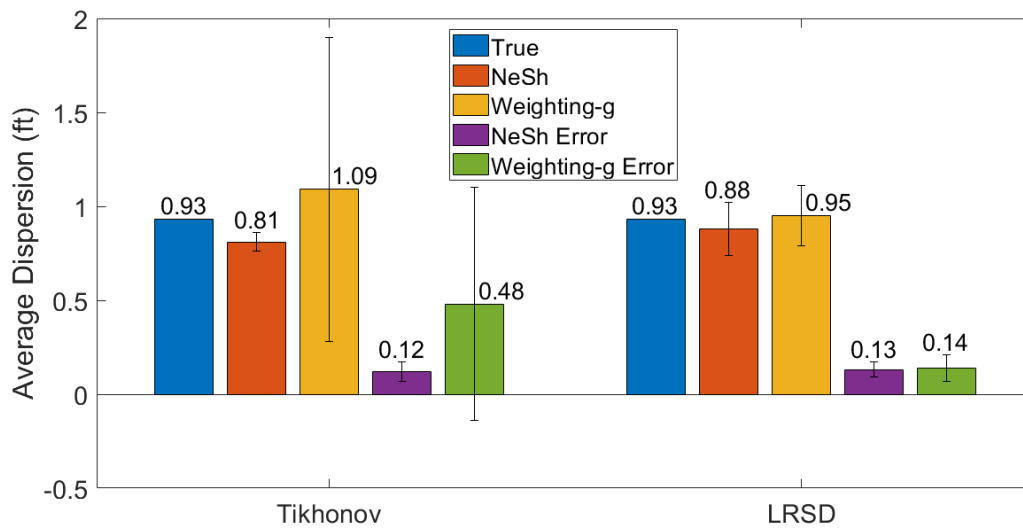


Figure 26: Graph of true dispersion, average dispersion, and average dispersion error results.

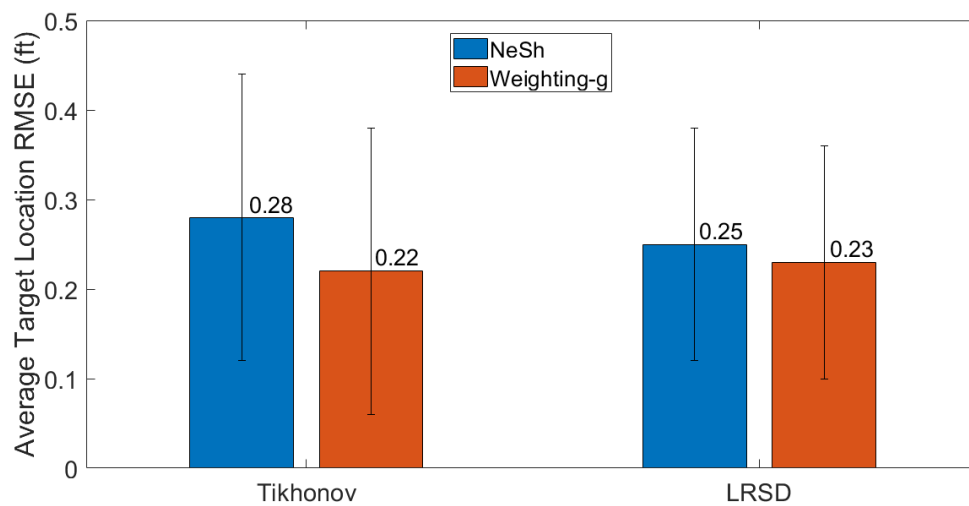


Figure 27: Graph of average target location RMSE results.

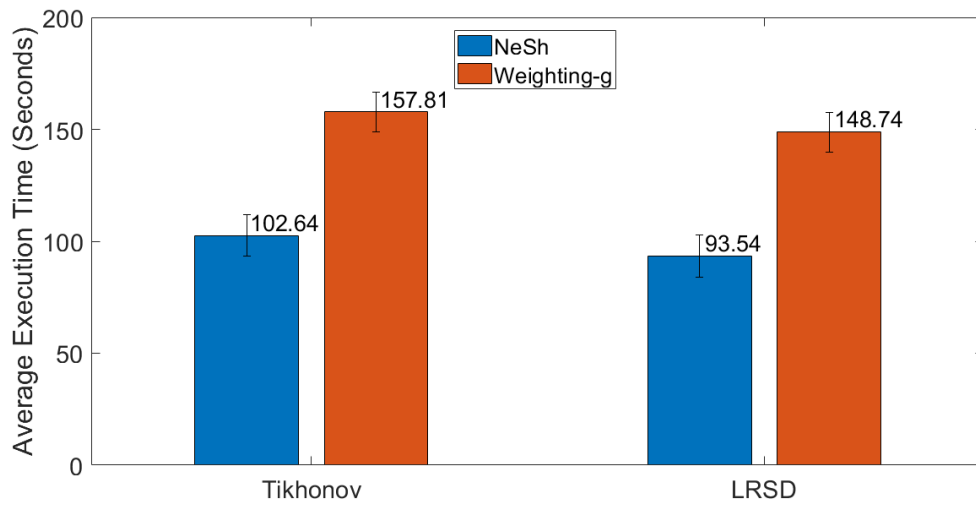


Figure 28: Graph of average execution time results.

## V. Conclusions

The work conducted in this thesis provided a comparative analysis between different RTI models and reconstruction methods that were selected based on their ability to mitigate multipath interference. The NeSh and weighting-g models successfully used an ellipse to determine the pixels that were included on the LOS paths of the node links. For these models, the pixels along the LOS paths were assigned weights greater than zero while the pixels along the NLOS paths were assigned weights of zero. The multipath interference along the NLOS paths was suppressed by assigning weights of zero. Tikhonov regularization was chosen based on its linearity and suppression of noise by minimizing the energy in the derivative image. LRSD was chosen based on its ability to suppress the multipath interference in the background image while enhancing the target-induced attenuation in the foreground image.

The NeSh and weighting-g models were implemented in conjunction with Tikhonov regularization and LRSD to form the following four combinations: NeSh in conjunction with Tikhonov regularization (N-T), weighting-g in conjunction with Tikhonov regularization (W-T), NeSh in conjunction with LRSD (N-L), and weighting-g in conjunction with LRSD (W-L). Out of these combinations, the N-T combination is the most commonly used. Algorithms were written to implement the combinations in MATLAB for six different target scenarios, three single target and three two-target.

For all six target scenarios, the qualitative analysis of the attenuation images revealed there was not a single combination that consistently outperformed all the others in terms of noise prevalence and target localization accuracy. The lack of a single combination outperforming the others suggested the attenuation images alone were not sufficient enough to determine the combination performances. Also, the high variability associated with visual inspection performed by different people led to the conclusion that the qualitative analysis was not accurate enough to stand alone or be

used to make concluding inferences.

Five reproducible quantitative metrics (image MSE, target location RMSE, dispersion, dispersion error, and execution time) were ultimately used to determine the performances of the RTI model and reconstruction method combinations. The average image MSE results revealed the N-T, W-T, and W-L combinations had the lowest MSE. The average dispersion results revealed the W-L combination had the most accurate dispersion when compared to the true target dispersion. The average dispersion errors revealed the N-T combination had the lowest average dispersion error. The average target location RMSE results revealed the W-T combination had the lowest average RMSE. Lastly, the average execution time results revealed the N-L combination had the fastest execution time. The average results of these five performance metrics revealed there was not a single combination that outperformed the others for at least three out of the five metrics. Therefore, the average results alone were not used to determine the optimum combination. Instead, a rating technique was implemented to generate four overall ratings, one for each combination.

The ratings were ultimately used to determine the best performing RTI model and reconstruction method combination out of the four considered. First to calculate the ratings, the average results of each performance metric were normalized on a scale from zero to one with zero indicating the best result. To normalize the four average results of each metric, the minimum average result was subtracted from all four of the average results and those differences were divided by the maximum difference. The average dispersion was normalized in a similar way, except there was an initial step to find the absolute value of the difference between the true target dispersion and average target dispersion. Next, the means were calculated across each combination's five normalized average results. Lastly, the means were rounded to the nearest hundredth to yield the following ratings: N-T (0.38), W-T (0.74), N-L (0.35), and W-L (0.26).

The W-L combination had the best rating of 0.26 which was the closest rating to zero.

In this thesis, the quantitative results revealed no single RTI model and reconstruction method combination outperformed the others across at least three out of the five performance metrics. Therefore, a rating technique was implemented to assign a value to each combination by taking the mean of its corresponding normalized average results. Comparing the ratings revealed the W-L combination had the lowest rating of 0.26. The lowest rating was also considered the best rating because it was closest to zero which corresponded to the best value on the normalization scale. In conclusion, the W-L combination performed optimally at locating human targets from the RTI attenuation images.

## 5.1 Future Work

This thesis provided a comparative analysis between four RTI model and reconstruction method combinations using previously collected data. The worked performed in this thesis can be expanded by the following tasks:

- Find additional models and reconstruction methods with the ability to mitigate multipath interference and then use them to create new RTI model and reconstruction method combinations
- Expand the total number of target scenarios to include three-target cases
- Explore other performance metrics to find one that can quantitatively assess noise prevalence in attenuation images
- Collect new RSS measurements for different target locations using the RTI system and implement the RTI combinations using the new data sets.

## Bibliography

1. J. Wilson and N. Patwari, "Radio tomographic imaging with wireless networks," *IEEE Transactions on Mobile Computing*, vol. 9, pp. 621–632, 2010.
2. J. Tan, Q. Zhao, X. Guo, X. Zhao, and G. Wang, "Radio tomographic imaging based on low-rank and sparse decomposition," *IEEE Access*, vol. 7, pp. 50 223–50 231, 2019.
3. N. Deshpande, E. Grant, and T. C. Henderson, "Target localization and autonomous navigation using wireless sensor networks - a pseudogradient algorithm approach," *IEEE Systems Journal*, vol. 8, pp. 93–103, 2014.
4. H. Yigitler, R. Jantti, O. Kaltiokallio, and N. Patwari, "Detector based radio tomographic imaging," *IEEE Transactions on Mobile Computing*, vol. 17, pp. 58–71, 2017.
5. O. Kaltiokallio, H. Yigitler, and R. Jantti, "A three-state received signal strength model for device-free localization," *IEEE Transactions on Vehicular Technology*, vol. 66, pp. 9226–9240, 2017.
6. J. Wilson and N. Patwari, "See-through walls: Motion tracking using variance-based radio tomography networks," *IEEE Transactions on Mobile Computing*, vol. 10, pp. 612–621, May 2011.
7. Y. Luo, K. Huang, X. Guo, and G. Wang, "A hierarchical RSS model for RF-based device-free localization," *Pervasive and Mobile Computing*, vol. 31, pp. 124–136, Sep 2016.
8. S. Xu, H. Liu, F. Gao, and Z. Wang, "Compressive sensing based radio tomographic imaging with spatial diversity," *Sensors (Switzerland)*, vol. 19, Feb 2019.

9. Y. Zheng and A. Men, "Through-wall tracking with radio tomography networks using foreground detection," *IEEE Wireless Communications and Networking Conference, WCNC*, pp. 3278–3283, 2012.
10. O. Kaltiokallio, M. Bocca, and N. Patwari, "Follow @grandma: Long-term device-free localization for residential monitoring," *Proceedings - Conference on Local Computer Networks, LCN*, pp. 991–998, 2012.
11. M. Moussa and M. Youssef, "Smart devices for smart environments: Device-free passive detection in real environments," *7th Annual IEEE International Conference on Pervasive Computing and Communications, PerCom 2009*, 2009.
12. C. R. Anderson, R. K. Martin, T. O. Walker, and R. W. Thomas, "Radio tomography for roadside surveillance," *IEEE Journal on Selected Topics in Signal Processing*, vol. 8, pp. 66–79, 2014.
13. M. Bocca, O. Kaltiokallio, and N. Patwari, "Radio tomographic imaging for ambient assisted living," *Communications in Computer and Information Science*, vol. 362 CCIS, pp. 108–130, 2013.
14. G. Nafziger, *Wireless Sensor Network Optimization for Radio Tomographic Imaging*. Master's thesis, ENG, AFIT, Wright-Patterson AFB, OH, Mar 2019.
15. J. Wilson and N. Patwari, "A fade-level skew-laplace signal strength model for device-free localization with wireless networks," *IEEE Transactions on Mobile Computing*, vol. 11, pp. 947–958, Jun 2012.
16. C. Zhu and Y. Chen, "Distance attenuation-based elliptical weighting-g model in radio tomography imaging," *IEEE Access*, vol. 6, pp. 34 691–34 695, Jun 2018.

17. Z. Wang, H. Su, X. Guo, and G. Wang, "Radio tomographic imaging with feedback-based sparse bayesian learning," *8th International Conference on Information Science and Technology, ICIST 2018*, pp. 50–56, Aug 2018.
18. Y. Guo, K. Huang, N. Jiang, X. Guo, Y. Li, and G. Wang, "An exponential-rayleigh model for RSS-based device-free localization and tracking," *IEEE Transactions on Mobile Computing*, vol. 14, pp. 484–494, Mar 2015.
19. R. K. Martin, A. Folkerts, and T. Heinl, "Accuracy vs. resolution in radio tomography," *IEEE Transactions on Signal Processing*, vol. 62, pp. 2480–2491, May 2014.
20. B. R. Hamilton, X. Ma, R. J. Baxley, and S. M. Matechik, "Propagation modeling for radio frequency tomography in wireless networks," *IEEE Journal on Selected Topics in Signal Processing*, vol. 8, pp. 55–65, 2014.
21. N. Patwari and P. Agrawal, "Nesh : A joint shadowing model for links in a multi-hop network," *Analysis*, pp. 2873–2876.
22. W. Ke, H. Zuo, M. Chen, and Y. Wang, "Enhanced radio tomographic imaging method for device-free localization using a gradual-changing weight model," *Progress In Electromagnetics Research*, vol. 82, pp. 39–48, 2019.
23. K. Huang, Y. Guo, X. Guo, and G. Wang, "Heterogeneous Bayesian compressive sensing for sparse signal recovery," *IET Signal Processing*, vol. 8, pp. 1009–1017, Dec 2014.
24. M. E. Tipping, "Sparse bayesian learning and the relevance vector machine," *Journal of Machine Learning Research*, vol. 1, pp. 211–244, 2001.
25. S. Ji, Y. Xue, and L. Carin, "Bayesian compressive sensing," *IEEE Transactions on Signal Processing*, vol. 56, pp. 2346–2356, 2008.

26. A. Edelstein and M. Rabbat, "Background subtraction for online calibration of baseline RSS in RF sensing networks," *IEEE Transactions on Mobile Computing*, vol. 12, pp. 2386–2398, 2013.
27. M. Piccardi, "Background subtraction techniques: A review," *Conference Proceedings - IEEE International Conference on Systems, Man and Cybernetics*, vol. 4, pp. 3099–3104, 2004.
28. A. Beck and M. Teboulle, "A fast iterative shrinkage-thresholding algorithm," *Society for Industrial and Applied Mathematics Journal on Imaging Sciences*, vol. 2, pp. 183–202, 2009.
29. M. Bocca, O. Kaltiokallio, N. Patwari, and S. Venkatasubramanian, "Multiple target tracking with RF sensor networks," *IEEE Transactions on Mobile Computing*, vol. 13, pp. 1787–1800, 2014.
30. C. Zhang and S. Xia, "K-means clustering algorithm with improved initial center," *Proceedings - 2009 2nd International Workshop on Knowledge Discovery and Data Mining, WKKD 2009*, pp. 790–792, 2009.
31. D. Arthur and S. Vassilvitskii, "k-means++: The advantages of careful seeding," in *Proceedings of the eighteenth annual ACM-SIAM symposium on Discrete algorithms*, p. 1027–1035, Nov 2007.
32. Z. Wang, L. Qin, X. Guo, and G. Wanga, "Dual radio tomographic imaging with shadowing-measurement awareness," *IEEE Transactions on Instrumentation and Measurement*, pp. 1–1, Oct 2019.
33. C. Vergara, *Multi-Sensor Data Fusion between Radio Tomographic Imaging and Noise Radar*. Master's thesis, ENG, AFIT, Wright-Patterson AFB, OH, Mar 2019.

34. S. Nannuru, Y. Li, Y. Zeng, M. Coates, and B. Yang, "Radio-frequency tomography for passive indoor multitarget tracking," *IEEE Transactions on Mobile Computing*, vol. 12, pp. 2322–2333, 2013.
35. O. Kaltiokallio, R. Jäntti, and N. Patwari, "ARTI: An Adaptive Radio Tomographic Imaging System," *IEEE*, 2015.
36. M. C. R. Talampas and K. S. Low, "An enhanced geometric filter algorithm with channel diversity for device-free localization," *IEEE Transactions on Instrumentation and Measurement*, vol. 65, pp. 378–387, Feb 2016.
37. Z. Cao, Z. Wang, H. Fei, X. Guo, and G. Wang, "Generative model based attenuation image recovery for device-free localization with radio tomographic imaging," *Pervasive and Mobile Computing*, vol. 66, Jul 2020.
38. J. Wilson and N. Patwari. Spin – TinyOS Code for RSS Collection. [Online]. Available: <http://span.ece.utah.edu/spin>

# REPORT DOCUMENTATION PAGE

*Form Approved*  
*OMB No. 0704-0188*

The public reporting burden for this collection of information is estimated to average 1 hour per response, including the time for reviewing instructions, searching existing data sources, gathering and maintaining the data needed, and completing and reviewing the collection of information. Send comments regarding this burden estimate or any other aspect of this collection of information, including suggestions for reducing this burden to Department of Defense, Washington Headquarters Services, Directorate for Information Operations and Reports (0704-0188), 1215 Jefferson Davis Highway, Suite 1204, Arlington, VA 22202-4302. Respondents should be aware that notwithstanding any other provision of law, no person shall be subject to any penalty for failing to comply with a collection of information if it does not display a currently valid OMB control number. **PLEASE DO NOT RETURN YOUR FORM TO THE ABOVE ADDRESS.**

<b>1. REPORT DATE (DD-MM-YYYY)</b> 25-03-2021		<b>2. REPORT TYPE</b> Master's Thesis		<b>3. DATES COVERED (From — To)</b> Sept 2019 — Mar 2021			
<b>4. TITLE AND SUBTITLE</b>  Mitigating the Multipath Effects on Radio Tomographic Imaging				<b>5a. CONTRACT NUMBER</b>			
				<b>5b. GRANT NUMBER</b>			
				<b>5c. PROGRAM ELEMENT NUMBER</b>			
				<b>5d. PROJECT NUMBER</b>			
				<b>5e. TASK NUMBER</b>			
<b>6. AUTHOR(S)</b>  Destinee N. Battle, 1 <sup>st</sup> Lt, USAF				<b>5f. WORK UNIT NUMBER</b>			
				<b>8. PERFORMING ORGANIZATION REPORT NUMBER</b>  AFIT-ENG-MS-21-M-012		<b>7. PERFORMING ORGANIZATION NAME(S) AND ADDRESS(ES)</b> Air Force Institute of Technology Graduate School of Engineering and Management (AFIT/EN) 2950 Hobson Way WPAFB OH 45433-7765	
						<b>9. SPONSORING / MONITORING AGENCY NAME(S) AND ADDRESS(ES)</b>  Intentionally Left Blank	
<b>10. SPONSOR/MONITOR'S ACRONYM(S)</b>  Intentionally Left Blank		<b>11. SPONSOR/MONITOR'S REPORT NUMBER(S)</b>		<b>12. DISTRIBUTION / AVAILABILITY STATEMENT</b> DISTRIBUTION STATEMENT A: APPROVED FOR PUBLIC RELEASE; DISTRIBUTION UNLIMITED.			
				<b>13. SUPPLEMENTARY NOTES</b>			
<b>14. ABSTRACT</b> Various radio tomographic imaging (RTI) models and reconstruction methods are equipped with capabilities to mitigate the effects of multipath interference. This thesis combined the network shadowing (NeSh) and weighting-g models in conjunction with Tikhonov regularization and low-rank and sparse decomposition (LRSD). MATLAB was used to implement the four combinations for six experimental data sets and produce attenuation images. The attenuation images were analyzed qualitatively and quantitatively to accomplish the goal of determining which combination performed best at locating human targets. After analyzing the results, it was determined that no single combination outperformed the others for at least three out of the five quantitative metrics. Therefore, a rating technique was used instead to normalize the average results of each metric and find the mean across each combination's newly normalized average results. In accordance with the normalization scale, the lowest and best rating revealed the optimum combination was the weighting-g model implemented in conjunction with LRSD.							
<b>15. SUBJECT TERMS</b>  Radio Tomographic Imaging							
<b>16. SECURITY CLASSIFICATION OF:</b>			<b>17. LIMITATION OF ABSTRACT</b>  UU	<b>18. NUMBER OF PAGES</b>  72	<b>19a. NAME OF RESPONSIBLE PERSON</b> Dr. Richard K. Martin, AFIT/ENG		
a. REPORT  U	b. ABSTRACT  U	c. THIS PAGE  U			<b>19b. TELEPHONE NUMBER (include area code)</b> (937) 255-3636, x4625; richard.martin@afit.edu		